Contents lists available at ScienceDirect

International Journal of Mechanical Sciences

Experimental and homogenized orientation-dependent properties of hybrid long fiber-reinforced thermoplastics

Benedikt M. Scheuring [a,*], Nicolas Christ [a,b], Juliane Blarr [a], Wilfried V. Liebig [a], Jörg Hohe [b], John Montesano [c], Kay A. Weidenmann [d]

[a] *Karlsruhe Institute of Technology, Institute for Applied Materials, Engelbert-Arnold-Straße 4, Karlsruhe, 76131, Germany*
[b] *Fraunhofer Institute for Mechanics of Materials IWM, Wöhlerstraße 11, Freiburg, 79108, Germany*
[c] *Composites Research Group, Department of Mechanical and Mechatronics Engineering, University of Waterloo, 200 University Ave West, Waterloo, N2L 3G1, Canada*
[d] *University of Augsburg, Institute of Materials Resource Management, Werner-von-Siemens-Straße 6, Augsburg, 86159, Germany*

ARTICLE INFO

ABSTRACT

This research presents a investigation of long fiber-reinforced thermoplastics (LFT) with mixed fiber types, combining experimental analysis with numerical modeling techniques. By accurately predicting the stiffness of mixed fiber composites, the design margin between mono fiber reinforced materials can be effectively exploited, facilitating the use of such materials. For this purpose in particular, a novel application of the Mori–Tanaka approach with two different inclusions guaranteeing symmetric stiffnesses is presented. This is a method that has never been used before in field studies. In addition, the study integrates fourth-order plate-averaged orientation tensors measured and subsequently interpolated to improve the accuracy of the modeling. Consistency with the established shear-lag modified Halpin–Tsai method is demonstrated, confirming the suitability of both approaches for predicting the tensile modulus of GF_{LFT} and $CF+GF_{LFT}$. However, discrepancies between predictions and experiments for CF_{LFT} are attributed to the complex microstructure of the material caused by bundling and poor dispersion of the CF. Furthermore, the study reveals remarkable hybridization effects within the mixed fiber LFT, particularly evident in the 22% increase in elongation at break observed in $CF+GF_{LFT}$ compared to CF_{LFT}. Overall, this research significantly advances the understanding and predictive capabilities regarding mixed fiber LFTs, which opens up a new design space of specific properties. This provides valuable insight for future research and industrial applications.

1. Introduction and state of the art

Owing to their high specific stiffness and strength properties, fiber-reinforced polymer (FRP) composites are widely established and used in various applications and areas such as the aircraft industry, automotive industry, medical technology, and sports equipment [1–3]. A wide variety of matrix materials, such as thermosets and thermoplastics are used, which can be reinforced with continuous fibers (Co) or discontinuous fibers (Dico) [4]. As reinforcing elements for DicoFRP, several types of fibers with different fiber properties are used. The most commonly used synthetic reinforcing fibers are glass fibers (GF) and increasingly also carbon fibers (CF). CFs are well suited for strong, stiff reinforcement with low density, but are very cost-intensive, exhibit brittle fracture behavior, and the ecological footprint in terms of CO_2 is large. GF in comparison to CF are cheaper and have better fracture properties, but their strength and stiffness are significant

lower [3,5,6]. Since the stricter regulations regarding emissions, e.g. in the automotive sector, brought weight reduction into focus and allow greater financial leeway, the demand for Dico-FRP with CF as reinforcement has increased in recent years [3,7]. A significant potential for structural component applications was demonstrated for thermoset based Dico-CFRP by combining both excellent mechanical properties and a complex formability [3,8]. These advantages are also obtained when using a thermoplastic matrix for Dico-CFRP, which additionally offers a solution for high-cycle production and recyclability [3,9, 10]. The long-fiber-reinforced-thermoplastic-direct-process (LFT-D), in which the fibers are directly fed as roving into a twin-screw extruder (TSE) together with the plasticized polymer from an upstream TSE (see Fig. 1), is particularly suitable as long as a critical fiber length is not compromised. In this way, the properties of the CF can be better exploited in the composite. [2,7,11,12]. In addition, the LFT-D is also
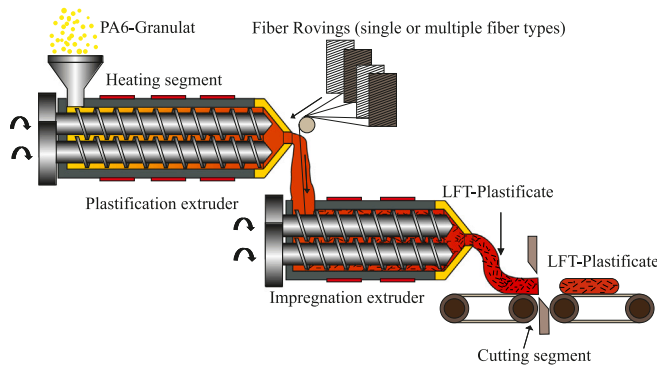

Fig. 1. Schematic drawing of the long-fiber-reinforced-termoplastic direct prozess (LFT-D) with two co-rotating twin-screw extruders (TSE) connected in series. The first for plasticizing and adding the polymer matrix and the second impregnating TSE in which the fiber rovings are broken up, split up and impregnated with the matrix.
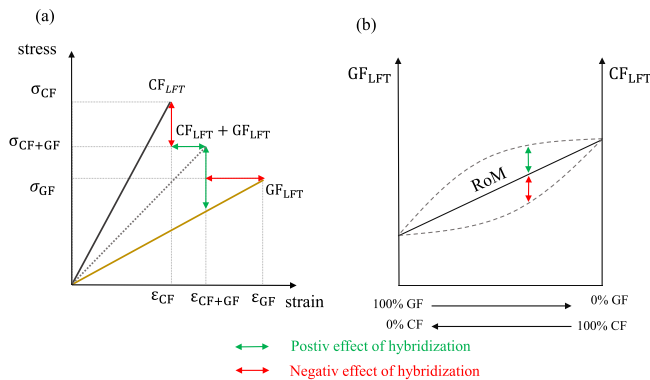

Fig. 2. Definition of the hybridization effect with (a) deviation of a distinct property of the hybrid with respect to one of the components (b) deviation from the "Rule of Mixture" (RoM) in positive or negative direction according to swolfs et al. [14].

suitable for the use of recycled fiber or mechanically recycled parts, which offers considerable advantages for recyclability [3].

Bondy et al. compression molded CF_{LFT} sheets in the LFT-D process, in which 25 vol.% of CF shows the best material properties for the composite [13]. In addition, they were able to show that a preferred fiber orientation in the flow direction is formed by the flow path, which in turn is clearly reflected in the mechanical properties [13]. However, in addition to their high cost, CF emit significantly more CO_2 during production than GF [5]. Furthermore, the brittle fracture behavior is still critical for crash relevant applications in automotive engineering. In these two aspects, GFs show significantly better properties. It is therefore not surprising that some attempts have been made to combine both glass and carbon fiber in a single composite. This allows the stiffness properties of CF composites to be combined with the fracture toughness properties of GF composites to form a stiff and tough hybrid material with moderate cost and CO_2 emissions. According to Swolfs, there are generally two ways to define the hybridization effect, as shown in Fig. 2 [14]. In Fig. 2(a), the hybridization effect is always given in terms of the deviation of a particular property from one of the individual components. According to Swolf et al. the elongation at fracture is of particular interest, since, for example, fibers of one component can withstand significantly higher elongations in the hybrid than in the monofiber composite [14]. Of course, the effect can be interpreted positively or negatively, depending on which of the components is taken as the basis. In Fig. 2(b) the hybridization effect is determined by the deviation of the rule of mixture (RoM), in which the properties of the hybrid result from the wighted sum of its individual components. A positive effect is defined when the property is better than the RoM, and

a negative effect when it is worse than the RoM. The RoM is defined in Eq. (1) with the tensile moduluf of elasticity ($E_{material}$) and the volume share of the individual components ($V_{material}$).

$$E_{CF+GF-LFT} = V_{GF-LFT} \cdot E_{GF-LFT} + V_{CF-LFT} \cdot E_{CF-LFT}. \qquad (1)$$

An important measure for distinguishing such composites is the type of fiber reinforcement and how they are dispersed [14–16]. Combinations of several fiber types in a composite were first investigated with continuous fibers and a thermoset matrix system and are usually called hybrid composites [17]. In these hybrid laminates, no positive hybridization effect according to definition (b) in Fig. 2 could be determined with respect to tensile modulus. The behavior of the materials in this case follows the RoM [17,18]. Kretsis et al. was able to confirm this and further shows that for hybrid laminates based on epoxy, both the compressive and flexural strength are below the RoM [16]. More promising results were obtained with the combination of fiber types in the category of discontinuous fiber-reinforced thermoplastics [6,19,20]. Fu and Lauke et al. were able to identify a positive hybridization effect in the tensile ultimate strength and elongation at break of a hybrid (CF+GF) short fiber-reinforced polypropylene based composite, while the tensile modulus of elasticity behaves according to the RoM [6]. The positive hybridization effect in terms of elongation at break can be explained as follows. Cracks that form at the ends of the carbon fibers do not lead to failure of the hybrid composites because the glass fibers act as crack arrestors [6]. This effect could be confirmed by Li et al. [21]. In addition, Fu and Mai et al. were able to demonstrate positive hybridization in the fracture toughness range for a similar hybrid [19]. Since the two fiber types interact at a very early stage of the LFT-D process and the relatively long fiber lengths allow the properties of both fibers to be optimally utilized, there is a lot of potential in a hybrid LFT-D composite. In a comparative process where glass and carbon fiber rovings were introduced into the polymer melt using a twin screw extruder, it was observed that the CF were longer and the GF were shorter compared to the single fiber composites [19]. Another particularly interesting aspect is the consideration of the fiber orientation induced by the flow path during molding. Since mechanical characterization is time-consuming, it is of particular interest to be able to adequately describe material parameters such as the stiffness of the hybrid material by means of a homogenization approach. Yan et al. were able to obtain good results for a short GF+CF reinforced PP with a two-step modified Halpin–Tsai based on the laminate analogy approach method [22]. Another method widely used in the field of Dico-FRP and which has shown very good results in the field of monofiber materials is the homogenization according to the Mori–Tanaka scheme [23,24].

In the present study, the interaction of a fiber mix of glass and carbon fibers with a polyamid 6 matrix in the LFT-D process and in subsequent extrusion is examined. Both the microstructure and the resulting mechanical properties in the tensile test are examined and hybridization effects could be detected. For this purpose, specimens with only one type of fiber as reinforcement are compared with a hybrid reinforced in equal parts with both fibers. Another focus is on the directionality of material behavior and its relationship to microstructure. Finally, different homogenization methods are applied to predict the stiffness of materials reinforced with only one type of fiber and the hybrid. The aim is to develop a methodology to predict the stiffness of hybrid LFTs with different fiber compositions. This should enable the fiber composition in hybrid composites to be adjusted to a desired stiffness.

2. Material and characterization method

This section provides a comprehensive overview of the materials used, the fabrication methodology, the microstructural and mechanical characterization, and the detailed approach and derivation of the modeling methods employed.
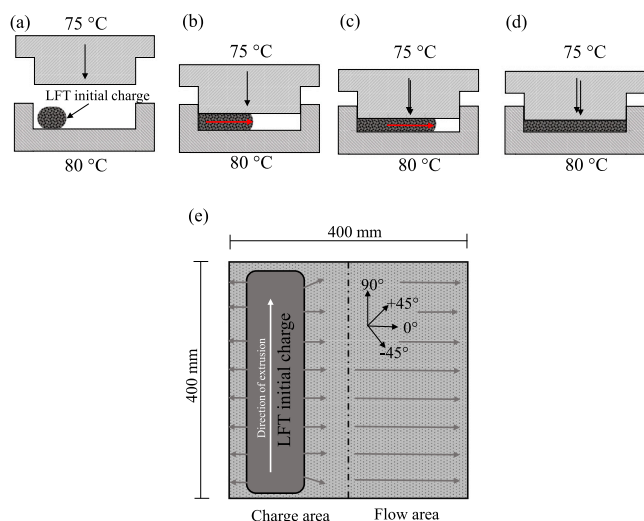
Fig. 3. (a-d) Compression molding process with side insert area of the initial charge and flow path, (e) position of the initial charge, division of the finished plate into charge and flow area and definition of the orientation relative to the flow path.

Fig. 4. Representative size, position and labeling of the fibercontent- (FVC), fiber length- (FLD) and fiber orientation- (FOD) specimen in a plate. "C" denotes a specimen out of charge area, "F" denotes a specimen out of flow area and "C-F" labels the intermediate zone. "1", "2" and "3" signify the position concerning the y-axis with "1" denoting the specimen with the highest absolute value of y (upper specimen).

2.1. Manufacturing and specimen preparation

The LFT-D plates were produced at the Fraunhofer ICT in Pfinztal, Germany, on a LFT-D machine (Dieffenbacher GmbH Maschinen- und Anlagenbau, Eppingen, Germany), which consists of two Leistritz twin-screw extruders (TSE). The first one is a Leistritz ZSE 40HP GL/32D with 55 kW power, in which the PA6 pellets are plasticized and homogenized with additives. The second is a Leistritz ZSE 40 GL/14.5D with 27 kW power, in which the plasticized PA6 (DOMO Technystar) and the fibers are added together and then mixed by the shear forces in the extruder (see Fig. 1). A detailed description of the screw geometries in both TSEs can be found in Schelleis et al. [25]. The glass fibers used in the process were StarRov® 895 2400 (Johns Manville) with a tex number of 2400 and the carbon fibers used were PX3505015W-61 (ZOLTEK) with a tex number of 3750. According to their data sheets, both fibers are particularly suitable for use with polyamides. All material types were produced with the same polymer flow rate of 25 kg/h and a design fiber volume content of 25%. The 3 mm thick sheets were pressed on a Dieffenbacher press (type DYL 630/500) using a polished steel tool with dimensions of 400 mm × 400 mm and a maximum pressure on the filled sheet of 200 bar. A side insert position was chosen so that a flow front is formed during the pressing process to fill the mold (see Fig. 3(a)–(d)). The finished sheet can thus be separated into two areas, the charge area and the flow area, as shown in Fig. 3(e). This classification is based on microstructural differences between the two regions, which are due to the structure of the initial charge. Further elaboration of this categorization is provided in Section 3.3.1. In addition, the different orientations with respect to the flow front are defined (see Fig. 3(e)), which were chosen as a reference for the later orientation-dependent characterization and homogenization.

Specimen were cut from the pressed plates in an iCUTwater smart of the company imes-icore with a pressure of 1500 bar, a cutting speed of 300 mm/min and a flow rate of 250 g/min of cutting sand Classic Cut 120 garnet of the company GMA. After cutting, the samples were dried in an oven at 50° C for at least 240 h. The samples were then hermetically sealed and additionally stored in an desiccator with silica gel to ensure that no moisture was absorbed during storage.

2.2. Microstructure investigation

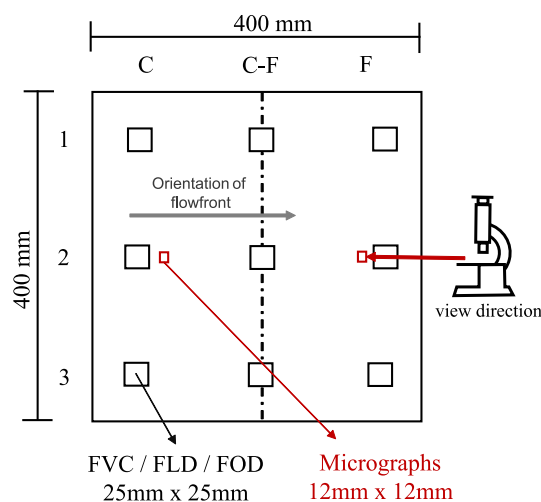This section explains the various microstructural investigations that were carried out on the different materials. In particular, the sampling positions and the methods used to determine the various characteristic values as well as the methods used to create micrographs and μCT images are discussed.

2.2.1. Fiber content and fiber length distribution

Fiber content measurements were performed at the Fiber Institute Bremen (FIBRE). The matrix of nine samples per material type with a dimension of 25 mm × 25 mm was exposed to sulfuric acid. Wet chemical removal of the matrix was chosen because preliminary tests in a TGA showed that ashing of the matrix without burning part of the carbon fibers could not always be guaranteed. All samples were previously scanned in the μ-CT (see Section 2.2.3) to enable fiber orientation measurements and to attribute variations in fiber volume content to possible fiber bundles. In order to visualize possible flow effects on fiber length and fiber content, three samples each were taken from the charge area, from the boundary between the charge and flow area, and from the flow area. The exact sampling locations are shown in Fig. 4. The fiber length distribution analysis was performed on the exposed fibers with FiberShape at FIBRE using a bright field for the GF and a dark field for the CF. To determine whether the individual fiber lengths in the theory exceed the critical fiber length (the fiber length above which a complete load transfer into the fiber is possible), formula (2) according to Kelly and Tyson [26] can be used, where σ_f is the tensile strength of the fiber, r is the fiber radius and τ_y is the interfacial shear strength

$$l_{\text{crit}} = \frac{\sigma_f \cdot r}{\tau_y}. \tag{2}$$

For the calculations in this work, the values for τ_y were taken from the literature (GF-PA6 from Kim et al. [27] (16.25 MPa)) (CF-PA6 from Zhu et al. [28] (ca. 46 MPa)). The values for σ_f and r were taken from the respective data sheets of the fibers.

2.2.2. Micrographs

For the micrographs, 12 mm ×12 mm specimens were taken from the flow and charge regions, respectively shown in Fig. 4. All micrographs were taken with the 0° orientation, i.e. the flow front, pointing out of the image plane as shown in Fig. 4. To make the fibers visible, the sample preparation for all materials was performed in 7 polishing steps based on the description of Sharman et al. [29]. The images were taken with a reflected light microscope, with multiple images being stitched together directly in the software.

Table 1
Scan parameters for the different material types.

Parameter	CF$_{LFT}$ and CF+GF$_{LFT}$	GF$_{LFT}$
Voltage/kV	110	125
Current/mA	0.13	0.12
Voxel size/μm	17.39	19.17
Linebinning parameter	2	2
Number of projections	2220	2100
Exposure/Integration time/ms	800	1000

2.2.3. X-ray computed tomography

For the microstructure investigations via μCT, the nine specimens per material system were used from Section 2.2.1 for which the positions and labeling can be seen in Fig. 4. The size and position of the specimen was chosen intentionally. Certainly, all three areas were to be covered. Beyond that, it was important not to choose locations too close to the edges. Areas near the borders usually show edge effects in the fiber orientation, which have little to do with the actual global orientation (cf. [30]). Since the determined fiber orientation tensors, or the fiber orientation distribution, are subsequently to be averaged over a plate and included in the homogenization calculation (more on averaging in Section 2.3.2), the CT samples should be chosen representatively and are therefore not located in edge regions. The size of the samples also results from experience, test runs and previous studies (cf. [30]). Thus, the samples must be large enough not to exclusively image a strongly locally deviating structure as well as to cover whole fibers and not to cut off bigger fiber lengths (cf. Section 3.1). In addition, they must be small enough to avoid an overly isotropic fiber orientation tensor that might not represent as much of a preferred direction. These considerations resulted in the size and position of the samples. The specimens were scanned in an YXLON-CT (Yxlon International CT GmbH, Hattingen, Germany) precision μCT system with a μ-focus X-ray transmission tube with tungsten target and a flat panel PerkinElmer (Waltham, MA, USA) Y.XRD1620 detector with 2048 pixel × 2048 pixel. Individual scan parameters were selected for each material in order to obtain the best possible images. The parameters are given in Table 1.

For the hybrid material and the purely carbon fiber reinforced polyamide 6, the same parameters were chosen. The object rotates 360° in the beam path in steps of $\varphi = 360°/n_{\text{projections}}$ (cf. Table 1). All of the projections were then reconstructed to a 3D volume by applying the Feldkamp cone-beam algorithm [31].

2.3. Fiber orientation

This section describes the methodology for determining fiber orientation from μCT data. It also explains the various processing steps required to use the fiber orientation in subsequent modeling.

2.3.1. Determination of fiber orientation via μCT

Fiber orientation tensors (FOT) were introduced by Advani and Tucker [32] as a compact and handy representation of fiber orientation distributions. The FOT of second and fourth order are commonly used most often:

$$\boldsymbol{A} = \int_{\mathcal{S}} \Psi(\boldsymbol{p}) \boldsymbol{p} \otimes \boldsymbol{p} \, d\boldsymbol{p}, \tag{3}$$

$$\mathbb{A} = \int_{\mathcal{S}} \Psi(\boldsymbol{p}) \boldsymbol{p} \otimes \boldsymbol{p} \otimes \boldsymbol{p} \otimes \boldsymbol{p} \, d\boldsymbol{p}, \tag{4}$$

where Ψ is the probability density of the fiber distribution, which is a function of the unit vector $\boldsymbol{p}$. The homogenization method by Mori–Tanaka described in Section 2.5.2 requires the FOT of fourth order of each material type. For the hybrid material two separate fiber orientation tensors for both the glass and the carbon fibers are needed. Additionally, in order to apply the Halpin–Tsai homogenization method

(cf. Section 2.5.3), the fiber orientation distribution (FOD) of the plates is required. For handling reasons, a discrete fiber orientation histogram is determined in this case.

All of the described values are determined through processing the acquired μCT images (cf. Section 2.2.3). In order to generate the FOT and FOD for each specimen, pre-processing steps were required. The reconstructed volumetric image is cut into regions of interest (ROI) of each specimen. After adjusting brightness and contrast, a median filter with a kernel size of 10 was applied to the images of the carbon fiber reinforced specimens only, as they showed more distinct noise. Subsequently, the grayscale value threshold, which separates fibers from matrix is determined. This process was straightforward for the pure CF and GF samples, however, it provided much more of a challenge for the hybrid specimen. The authors used a multiple thresholding procedure in order to separate the different fiber types. Due to their better contrast towards the matrix, the glass fibers were thresholded first. The resulting image stack was subtracted from the original one. Subsequently, the air is thresholded and the resulting image stack is again subtracted from the original stack, leaving air as completely black areas and glass as completely white. Then, a twofold limited threshold was used cutting off air (black), glass (white) and matrix, which was closest to the carbon fibers. The threshold along with the stack was fed to a C++ code implemented by Pinter et al. [33] creating a vector-valued image with the orientations per voxel. The code implemented with the help of the ITK library [34,35], uses the structure tensor as it performed best out of three methods as a robust, first numerical derivative based approach. In more detail, the image gradients are calculated firstly, combined with a Gaussian blur of a width of σ ($\sigma = 0.2$ in this study). The tensor resulting from the dyadic product of the gradient in each voxel,

$$\nabla I_\sigma(\mathbf{x}) \otimes \nabla I_\sigma(\mathbf{x}) = \begin{bmatrix} \left(\dfrac{\delta I_\sigma}{\delta x}\right)^2 & \dfrac{\delta I_\sigma}{\delta x}\dfrac{\delta I_\sigma}{\delta y} & \dfrac{\delta I_\sigma}{\delta x}\dfrac{\delta I_\sigma}{\delta z} \\[2mm] \dfrac{\delta I_\sigma}{\delta y}\dfrac{\delta I_\sigma}{\delta x} & \left(\dfrac{\delta I_\sigma}{\delta y}\right)^2 & \dfrac{\delta I_\sigma}{\delta y}\dfrac{\delta I_\sigma}{\delta z} \\[2mm] \dfrac{\delta I_\sigma}{\delta z}\dfrac{\delta I_\sigma}{\delta x} & \dfrac{\delta I_\sigma}{\delta z}\dfrac{\delta I_\sigma}{\delta y} & \left(\dfrac{\delta I_\sigma}{\delta z}\right)^2 \end{bmatrix}, \tag{5}$$

is perpendicular to the gradient or the fiber surface, respectively. Subsequently, all tensors are averaged by another Gaussian blur with the standard deviation ρ:

$$\mathbf{J}_\rho(\mathbf{x}) = G(\nabla I_\sigma(\mathbf{x}) \otimes \nabla I_\sigma(\mathbf{x}), \rho). \tag{6}$$

The blurring parameter ρ was 8 in this work. Especially for the carbon fibers, evaluating a larger image region to determine the orientation at a certain point, seemed reasonable. This tensor again is perpendicular to the local fiber orientation and by evaluating the smallest eigenvalue of the tensor and its corresponding eigenvector, the fiber orientation can be calculated.

The vector-valued image with the orientations per voxel is in the format of a .raw-file and corresponding meta data file (.mhd). Proceeding from this file, multiple evaluations were conducted with MATLAB. The fiber orientation tensor of second order is evaluated by summing up the element-by-element multiplication (using the .* Operator in MATLAB) of two channels of the image over all voxels (e.g. for the a_{11} component, the multiplication of the voxel values of the first channel with itself is needed, for a_{12} the first and second channel are used, etc.). Subsequently, the orientation tensor is normalized with the trace. For the determination of the fourth level orientation tensors, an analogous procedure is followed (provided that four factors per component and the different trace are used). The course of the main components of the FOT over the thickness of each specimen is evaluated as well in order to detect process-induced skin and core layers concerning orientation. After transforming matrix data to point data, the occurring angles θ can be determined by using the four-quadrant inverse tangent. The angles are only evaluated between 0° and 180°, hence 0 and π, as the rest of the distribution is symmetric. The data of θ is partitioned into $n_{centers} = $

20 centers with an interval arc length of $n_i \in [i \cdot \pi/20, (i+1) \cdot \pi/20]$ with $i = \{x \in \mathbb{N}_0 : x < 20\}$ and it is counted how often this angle group appears in the specimen in order to obtain a discrete fiber orientation histogram.

2.3.2. Fourth order fiber orientation tensor interpolation

The simple component averaging of the nine determined FOT resulted in an averaged tensor which did not represent the fiber orientation of the entire plate sufficiently well (cf.). The authors ascribe this phenomenon to the localized information points. However, interpolating the measured tensors and generating a more holistic orientation field of the entire plate constitutes a solution with limited additional expenses. This has been done by Blarr et al. before for tensors of second order (cf. [30,36,37]). In the mentioned paper [30], the decomposition approach is used to generate 160 tensors by interpolating nine tensors of a plate. The authors applied this procedure analogously herein. The plate was divided into 13×13 positions with the measured tensors placed at the nine possible combinations of the coordinates 2, 7 and 12. In contrast to the cited paper, the measured tensors – hence the cut out specimens – were not located at the edge positions of 1, 7 and 13. Likewise deviating, the authors averaged the 169 tensors at the end, since one tensor per plate configuration was needed for the homogenization. Indeed, the averaged tensor was closer to the experimental results and the plate orientation distribution. In order to use these averaged tensors for the Mori–Tanaka approach, a closure approximation had to be used. The authors tested both the quadratic and the invariant based optimal fitting (IBOF) closure approximations with non-optimal results. It has been shown before that closure approximations do not produce sufficiently accurate results when predicting mechanical properties [38,39]. It was therefore desired to interpolate the fourth level tensors directly.

The implemented decomposition approach in Blarr et al. is based on the eigenvalue problem [30]:

$$\boldsymbol{A}\boldsymbol{p}_i = \lambda_i \boldsymbol{p}_i. \tag{7}$$

It can be rewritten using a tensor built from the eigenvectors $\boldsymbol{p}_i$ as column vectors. If the eigenvectors are normalized, this tensor is denoted as the rotation matrix $\boldsymbol{R}$, yielding:

$$\boldsymbol{A} = \boldsymbol{R}\boldsymbol{\Lambda}\boldsymbol{R}^{-1}. \tag{8}$$

The inverse of $\boldsymbol{R}$ is identical to its transpose $\boldsymbol{R}^T = \boldsymbol{R}^{-1}$ thanks to its orthogonality:

$$\boldsymbol{A} = \boldsymbol{R}\boldsymbol{\Lambda}\boldsymbol{R}^T = \boldsymbol{R} \star \boldsymbol{\Lambda}. \tag{9}$$

After decomposing the measured tensors, the part determining the orientation, hence the rotation matrix, and the part causing the shape of the tensor, hence the eigenvalues, can be weighted individually depending on their distance to the position of the tensor that is to be determined. The motivation for this decomposition instead of simply weighting the tensor components directly is explained in the mentioned publication [30]. Blarr et al. then converted the rotation matrix to quaternions and instead of the eigenvalues, another kind of invariant set is used, before the weighting. Following, the weighted quaternions and invariants are reassembled to the interpolated tensor.

This decomposition approach was made use of with the novelty of transferring the methods to tensors of fourth order. Therefore, the tensors were read in Mandel notation and subsequently decomposed into eigenvalues (6×1) and the rotation matrix (6×6) using NumPy's linalg library [40]. The eigenvalues were sorted by magnitude. It was made use of the fact that portraying a 3D tensor in 2D using Mandel notation and hence receiving a 6×6 matrix, allows the authors to use the spectral decomposition. The following transformation to quaternions and orthogonal invariants was not considered for the interpolation of tensors of fourth order in this publication as the transformation is not straightforward. Hence, the rotation matrix and eigenvalues are used directly. Following, the distance-dependent weights applied to each measured tensor for each tensor position to be determined were calculated through Shepard's inverse distance weighting [41]:

$$w_i = \frac{1}{\|\boldsymbol{x}_i - \boldsymbol{x}\|^p} \frac{1}{\sum_j \|\boldsymbol{x}_j - \boldsymbol{x}\|^{-p}}. \tag{10}$$

The weights are the inverse of the distance between the interpolation location $\boldsymbol{x}$ and the sample points $\boldsymbol{x}_i$, raised to the power p, a positive real number, called the power parameter, which is set to 2 in this work. The eigenvalues and the rotation matrices were directly weighted individually for each point. The final interpolated orientation tensor for a specific point was obtained through reassembly of the newly weighted rotation matrix and eigenvalues to a then interpolated tensor.

2.4. Tensile tests

Tensile tests were performed according to DIN EN ISO 527–4 2020 on a Zwick Roell Universal testing machine equipped with a 20 kN load cell and a commercially available digital image correlation system (GOM-Aramis 4M Adjustable) to record strain. From all materials (CF_{LFT}, GF_{LFT}, $CF + GF_{LFT}$), for both areas (charge area, flow area) and for each orientation ($0°$, $\pm 11.25°$, $\pm 22.5°$, $\pm 45°$, $90°$), eight specimens were tested, of which only those that failed in the valid gauge length were considered for further evaluation. Rectangular specimen measuring 200 mm $\times$ 15 mm was selected as the specimen geometry and clamped between hydraulic clamping jaws with a free measuring length of 100 mm. The test was carried out with a test speed of 2 mm/min. In order to use real matrix properties for modeling, tensile tests were performed on samples of injection molded pure PA6 using the same methodology and geometry. Young's modulus E_{11} and Poisson's ratio v_{12} were determined.

2.5. Homogenization procedure

The main motivations to use homogenization methods are to find expressions for material properties in composite materials which are otherwise too complicated or time consuming to describe and calculate in full detail and to reduce expenses in experimental and computational efforts [42]. Homogenization methods are used to retrieve analytical expressions, numerical results or theoretical bounds for effective material properties when the underlying micro-structure is of multi-phase and/or inhomogeneous type and usually outline the field of micromechanics. Introductory material can be found for general composites in [43,44], more specifically in the field of fiber reinforced composites in [45, p. 341 ff.], and in a very condensed form in [46].

Concerning stiffness properties, first useful results in terms of bounds were developed by Voigt (cf. [47]) and Reuss (cf. [48]) in 1889 and 1929, respectively [49, p. 296]. These are easily implemented bounds and deliver a first approximation for effective properties. The downside of this bounding approach is that the resulting envelope of effective properties is broad, once the volume fraction of one phase exceeds a dilute inclusion. Also, a common misconception is that the Voigt bound for material properties, such as Young's modulus and Poisson's ratio in isotropic materials are given with the simple rule of mixture [50, p. 2198], while this is only valid for shear and bulk modulus [46, p. 12]. Bounding methods of higher order and better precision can be found in the Hashin–Shtrikman variational scheme, though the calculation depends non-linearly on a reference material, which must be chosen by the user [23, p. 3785 ff.].

Besides bounding methods, analytical expressions to pinpoint the effective properties are found with the so called mean-field approximations, which are built upon Eshelby's solution [51]. These methods ought to be within the variational bounds to be physically meaningful. Such methods are the dilute distribution, the Mori–Tanaka and the self-consistent scheme, of which the Mori–Tanaka and self-consistent scheme are the most popular among them [42]. The simple

self-consistent scheme is not evaluated in this work due to a lack of motivation in embedding an inclusion into the effective medium [52]. The generalized version, in which a three-phase body of inclusion, matrix and effective material is analyzed, was also not considered due to a dependence of the effective properties on the initial stiffness for the iteration process. Furthermore, it was shown that the self-consistent method gives a sufficient prediction of the behavior of polycrystals but it is less accurate in the case of two-phase composites as shown by [53]. Recent research applying a multi-inclusion self-consistent homogenization to porous polycrystals can be found in [54] and [55].

2.5.1. Derivation of the homogenization equation

By applying the average stress/strain theorem, it is easily shown that the general equation for the effective stiffness is

$$\bar{\mathbb{C}} = \frac{1}{V} \int_V \mathbb{C}\mathbb{A} \, dV = \sum_{i=1}^{n} c_i \frac{1}{V_i} \int_{V_i} \mathbb{C}\mathbb{A} \, dV$$

$$= \langle \mathbb{C}\mathbb{A} \rangle = \sum_{i=1}^{n} c_i \langle \mathbb{C}\mathbb{A} \rangle_i, \tag{11}$$

where $\bar{\mathbb{C}}$ and $\mathbb{C}$ are the effective stiffness and local stiffness, respectively, n represents the number of individual constituents and c_i is the relative volume fraction of a domain of constant phase. $\langle \cdot \rangle$ and $\langle \cdot \rangle_i$ indicate the volume averages of the total volume and the volume of phase i, respectively. $\mathbb{A}$ is defined as a linear mapping of the effective strain $\bar{\varepsilon}$ to the local strain ε called concentration or localization tensor

$$\varepsilon = \mathbb{A}\bar{\varepsilon}. \tag{12}$$

When the constituents are split into a matrix phase (subscript m) and fibrous phase (subscript f), without further splitting the specific type of fiber, Eq. (11) reduces to

$$\bar{\mathbb{C}} = c_m \langle \mathbb{C}\mathbb{A} \rangle_m + c_f \langle \mathbb{C}\mathbb{A} \rangle_f. \tag{13}$$

It can be shown that the volume average of the concentration tensor must be equal to the identity tensor of fourth order, which allows to express the volume average of the concentration tensor in one phase as a function of the other

$$c_m \langle \mathbb{A} \rangle_m = \mathbb{I} - c_f \langle \mathbb{A} \rangle_f. \tag{14}$$

Together, Eqs. (13) and (14), give the general homogenization equation for a material consisting of a matrix and fibrous phase

$$\bar{\mathbb{C}} = \mathbb{C}_m + c_f \langle (\mathbb{C}_f - \mathbb{C}_m)\mathbb{A} \rangle_f. \tag{15}$$

2.5.2. Mori–Tanaka

The starting point for the Mori–Tanaka (MT) scheme is the single inclusion problem (SIP) after Eshelby (cf. [51]). In alignment with [56], it can be shown that for the SIP with a spheroid inclusion the relation between local strain within an α-type inclusion $\varepsilon_{f,\alpha}$ and the effective strain $\bar{\varepsilon}$ is

$$\varepsilon_{f,\alpha} = \underbrace{\left(\mathbb{I} + \mathbb{S}_\alpha \mathbb{C}_m^{-1}(\mathbb{C}_{f,\alpha} - \mathbb{C}_m) \right)^{-1}}_{=\mathbb{A}_{f,\alpha}^\infty} \bar{\varepsilon}, \tag{16}$$

where $\mathbb{I}$ and $\mathbb{S}_\alpha$ are the identity tensor and the spheroid Eshelby tensor of fourth order, respectively, and $\mathbb{C}_m$ and $\mathbb{C}_{f,\alpha}$ are the fourth order stiffness tensors of matrix and inclusion of type α.

The assumption in the MT approach is that the Eshelby solution in Eq. (16) can be used to approximate a mapping from the local matrix strain ε_m to the local fibrous strain $\varepsilon_{f,\alpha}$ of fiber type α

$$\varepsilon_{f,\alpha} = \mathbb{A}_{f,\alpha}^\infty \varepsilon_m. \tag{17}$$

Eq. (17) is then expressed as a function of the effective strain by incorporating another concentration tensor $\mathbb{A}_m^{MT}$ which maps the effective strain on the matrix strain

$$\varepsilon_m = \mathbb{A}_m^{MT}\bar{\varepsilon}, \tag{18}$$

so that Eq. (17) becomes

$$\varepsilon_{f,\alpha} = \underbrace{\mathbb{A}_{f,\alpha}^\infty \mathbb{A}_m^{MT}}_{=\mathbb{A}_{f,\alpha}^{MT}} \bar{\varepsilon}. \tag{19}$$

In analogy to Eq. (14), volume averaging of the local concentration tensor gives

$$\langle \mathbb{A}^{MT} \rangle = c_m \langle \mathbb{A}^{MT} \rangle_m + c_f \langle \mathbb{A}^{MT} \rangle_f,$$

$$= c_m \mathbb{A}_m^{MT} + c_f \sum_\alpha c_\alpha \mathbb{A}_{f,\alpha}^{MT} \stackrel{!}{=} \mathbb{I}, \tag{20}$$

where c_α is the volume fraction of the fibers of type α in relation to the total fiber volume with the condition that $\sum_\alpha c_\alpha = 1$. Here it is assumed that the properties are phase-wise constant. Inserting the definition of $\mathbb{A}_{f,\alpha}^{MT}$ from Eq. (19) and rearranging gives

$$\mathbb{A}_m^{MT} = \left(c_f \langle \mathbb{A}_{f,\alpha}^\infty \rangle_f + c_m \mathbb{I} \right)^{-1}. \tag{21}$$

Thus, an analytical expression for $\mathbb{A}_{f,\alpha}^{MT}$ is found and can be plugged into the general homogenization equation (Eq. (15))

$$\bar{\mathbb{C}}^{MT} = \mathbb{C}_m + c_f \langle (\mathbb{C}_{f,\alpha} - \mathbb{C}_m)\mathbb{A}_{f,\alpha}^{MT} \rangle_f,$$

$$= \mathbb{C}_m + c_f \langle (\mathbb{C}_{f,\alpha} - \mathbb{C}_m)\mathbb{A}_{f,\alpha}^\infty \rangle_f \left(c_f \langle \mathbb{A}_{f,\alpha}^\infty \rangle_f + c_m \mathbb{I} \right)^{-1}. \tag{22}$$

This expression needs to be handled with caution, since it was shown by [57,58] that a symmetric effective stiffness is not guaranteed for a multi-inclusion material, depending on the shape and stiffness properties of the different types of inclusion. Furthermore, for a hybrid material with differently shaped and oriented inclusions it was shown by [57] that the MT approach results in an effective stiffness which may lie outside the Hashin–Shtrikman-Walpole bounds.

Eq. (22) can be rearranged to give

$$\bar{\mathbb{C}}^{MT} = \left(c_m \mathbb{C}_m + c_f \langle \mathbb{C}_{f,\alpha} \mathbb{A}_{f,\alpha}^\infty \rangle_f \right) \mathbb{A}_m^{MT}, \tag{23}$$

which is equivalent to the form given in [59]. This formulation assumes that all inclusions are unidirectionally aligned (UD). If all fiber types can be described by a single fiber orientation distribution, i.e. all types of fibers are indistinguishably distributed, it is suitable to calculate an average effective stiffness by weighting the effective stiffness in Eq. (23) by the fiber orientation tensors of second and fourth order, as it was shown in [60, p. 40 ff.]. In contrast, when the types of fibers are individually distributed, Eq. (23) needs to be reformulated to

$$\bar{\mathbb{C}}^{MT} = \left(c_m \mathbb{C}_m + c_f \langle \{\mathbb{C}_{f,\alpha} \mathbb{A}_{f,\alpha}^\infty \} \rangle_f \right) \left(c_m \mathbb{I} + c_f \langle \{\mathbb{A}_{f,\alpha}^\infty \} \rangle_f \right), \tag{24}$$

where $\{\cdot\}$ indicates the orientation average [59]. The calculation of this orientation average is explained in [61] after Eq. (58), which is in reference to [32].

When there is only a single type of inclusion, $\mathbb{A}_{f,\alpha}^\infty$ and $\mathbb{C}_{f,\alpha}$ reduce to $\mathbb{A}_f^\infty$ and $\mathbb{C}_f$, respectively, and Eq. (22) simplifies to

$$\bar{\mathbb{C}}^{MT} = \mathbb{C}_m + c_f (\mathbb{C}_f - \mathbb{C}_m) \left(c_f \mathbb{I} + c_m \mathbb{A}_f^{\infty -1} \right)^{-1}. \tag{25}$$

The mentioned possibility that the MT homogenization can lead to stiffness tensors that do not contain the major symmetry was addressed in [62]. This is particularly useful when homogenizing hybrid materials, as is the case for glass and carbon fiber reinforced PA6 in this study. The result in [62] gives an alternate formulation

$$\bar{\mathbb{C}}^{MT} = \mathbb{C}_m + c_f \left(c_m \langle \{(\mathbb{C}_{f,\alpha} - \mathbb{C}_m)\mathbb{A}_{f,\alpha}^\infty \}\rangle_f^{-1} \right.$$

$$\left. + c_f \underbrace{\langle \{\mathbb{A}_{f,\alpha}^\infty \}\rangle_f \langle \{(\mathbb{C}_{f,\alpha} - \mathbb{C}_m)\mathbb{A}_{f,\alpha}^\infty \}\rangle_f^{-1}}_{=\mathbb{Z}} \right)^{-1}, \tag{26}$$

in which the latter term in the parenthesis $\mathbb{Z}$ is symmetrized to give

$$\bar{\mathbb{C}}^{MT} = \mathbb{C}_m + c_f \left(c_m \langle \{(\mathbb{C}_{f,\alpha} - \mathbb{C}_m)\mathbb{A}_{f,\alpha}^\infty \}\rangle_f^{-1} \right.$$

$$+ \frac{c_f}{2}(\mathbb{Z} + \mathbb{Z}^\mathsf{T})\Big)^{-1}. \tag{27}$$

Here we extended the formulation in [62] for an orientation average within the volume average to account for fiber orientation distributions. Again, the volume average is calculated as described in [61]. This formulation always results in major symmetric stiffness tensors. To ensure that the resulting stiffness tensors contain the major symmetry, the formulation in Eq. (27) is used in this study.

2.5.3. Halpin–Tsai model

A more simple, purely scalar and semi-empirical method to predict the effective properties of a composite is the Halpin–Tsai model, after [63]. In its original form, the model is used to predict the effective, elastic stiffness properties of unidirectional short fiber composites. According to [20], the equations in the Halpin–Tsai model are given with

$$E_\mathsf{L} = \frac{1 + 2(l/d)\eta_\mathsf{L} c_f}{1 - \eta_\mathsf{L} c_f} E_\mathsf{m}, \tag{28a}$$

$$E_\mathsf{T} = \frac{1 + 2\eta_\mathsf{T} c_f}{1 - \eta_\mathsf{T} c_f} E_\mathsf{m}, \tag{28b}$$

$$\nu_\mathsf{LT} = \nu_f c_f + \nu_\mathsf{m} c_\mathsf{m}, \tag{28c}$$

$$\nu_\mathsf{TL} = \frac{E_\mathsf{T}}{E_\mathsf{L}} \nu_\mathsf{LT}, \tag{28d}$$

$$G_\mathsf{LT} = \frac{1 + \eta_\mathsf{G} c_f}{1 - \eta_\mathsf{G} c_f} G_\mathsf{m}, \tag{28e}$$

where

$$\eta_\mathsf{L} = \frac{E_f/E_\mathsf{m} - 1}{E_f/E_\mathsf{m} + 2(l/d)}, \tag{29a}$$

$$\eta_\mathsf{T} = \frac{E_f/E_\mathsf{m} - 1}{E_f/E_\mathsf{m} + 2}, \tag{29b}$$

$$\eta_\mathsf{G} = \frac{G_f/G_\mathsf{m} - 1}{G_f/G_\mathsf{m} + 1}. \tag{29c}$$

With the calculated constants given in Eq. (28), the effective, planar stress–strain relation with the symmetry of transverse isotropy can be constructed, which is

$$\begin{bmatrix} \sigma_1 \\ \sigma_2 \\ \tau_{12} \end{bmatrix} = \underbrace{\begin{pmatrix} C_{11} & C_{12} & C_{16} \\ C_{12} & C_{22} & C_{26} \\ C_{16} & C_{26} & C_{66} \end{pmatrix}}_{=C_{ij}} \begin{bmatrix} \varepsilon_1 \\ \varepsilon_2 \\ \gamma_{12} \end{bmatrix}, \tag{30}$$

where the principal stress directions are aligned with the principal fiber directions in accordance to [64]. The components of the stiffness tensor are given with

$$C_{11} = \frac{E_\mathsf{L}}{1 - \nu_\mathsf{LT}\nu_\mathsf{TL}}, \tag{31a}$$

$$C_{12} = \nu_\mathsf{TL} C_{11}, \tag{31b}$$

$$C_{16} = 0, \tag{31c}$$

$$C_{22} = \frac{E_\mathsf{T}}{1 - \nu_\mathsf{LT}\nu_\mathsf{TL}}, \tag{31d}$$

$$C_{26} = 0, \tag{31e}$$

$$C_{66} = G_\mathsf{LT}. \tag{31f}$$

With the theory of linear elasticity [65], the stress–strain relation in any off-axis system rotated around the third principal axis is expressed as

$$\begin{bmatrix} \sigma'_1 \\ \sigma'_2 \\ \tau'_{12} \end{bmatrix} = \underbrace{\begin{pmatrix} C'_{11} & C'_{12} & C'_{16} \\ C'_{12} & C'_{22} & C'_{26} \\ C'_{16} & C'_{26} & C'_{66} \end{pmatrix}}_{=C'_{ij}} \begin{bmatrix} \varepsilon'_1 \\ \varepsilon'_2 \\ \gamma'_{12} \end{bmatrix}, \tag{32}$$

with the transformed stiffness components

$$\begin{bmatrix} C'_{11} \\ C'_{22} \\ C'_{12} \\ C'_{66} \\ C'_{16} \\ C'_{26} \end{bmatrix} = \begin{pmatrix} c^4 & s^4 & 2c^2s^2 & 4c^2s^2 \\ s^4 & c^4 & 2c^2s^2 & 4c^2s^2 \\ c^2s^2 & c^2s^2 & c^4 + s^4 & -4c^2s^2 \\ c^2s^2 & c^2s^2 & -2c^2s^2 & (c^2 - s^2)^2 \\ c^3s & -cs^3 & cs^3 - c^3s & 2(cs^3 - c^3s) \\ cs^3 & -c^3s & c^3s - cs^3 & 2(c^3s - cs^3) \end{pmatrix} \begin{bmatrix} C_{11} \\ C_{22} \\ C_{12} \\ C_{66} \end{bmatrix}, \tag{33}$$

where $c = \cos\theta$ and $s = \sin\theta$.

The authors would like to note that Eq. (32) is given in the Voigt notation, for which the rotation matrix is given in Eq. (33). This is justified by the fact that most reference works use this very notation. All homogenization procedures used in this paper are published in the Python package HomoPy (cf. [66]), which uses the normalized Voigt notation instead.

2.5.4. Shear-lag modified Halpin–Tsai model

To the best of the authors' knowledge, the incorporation of Cox' shear-lag model into the Halpin–Tsai model was first used in [64], which is motivated by a more physical approach to express the stiffness in the fiber direction in contrast to the classical, semi-empirical Halpin–Tsai model.

Cox introduced his model in [67] to analyze the effect of the fiber orientation on the stiffness properties in fibrous materials. A detailed derivation is given in [20, p. 140 ff.], which results in

$$E_\mathsf{L} = E_f c_f \left(1 - \frac{\tanh(\xi l/2)}{\xi l/2} \right) + E_\mathsf{m}(1 - c_f) \tag{34}$$

for the stiffness in fiber direction of a unidirectional short fiber-reinforced polymer, where l is the average fiber length. ξ is given by

$$\xi = \sqrt{\frac{2G_\mathsf{m}}{r_f^2 E_f \ln(R/r_f)}}, \tag{35}$$

where r_f is the average fiber radius and R is the mean separation of the fibers normal to their length. A hexagonal fiber packing gives

$$\ln\left(\frac{R}{r_f}\right) = \frac{1}{2} \ln\left(\frac{2\pi}{\sqrt{3}c_f}\right), \tag{36}$$

whereas a square fiber packing results in

$$\ln\left(\frac{R}{r_f}\right) = \frac{1}{2} \ln\left(\frac{\pi}{c_f}\right). \tag{37}$$

The longitudinal stiffness E_L from Eq. (34) is then used in the set of Eq. (28), instead of Eq. (28a), to give the shear-lag modified Halpin–Tsai equations. Fig. 5 compares the planar Young's modulus bodies (cf. [68]) for the classical Halpin–Tsai model with the shear-lag modified Halpin–Tsai model for identical material parameters.

2.5.5. Classical laminate theory

In order to include individual fiber types and distributions of the composite material using the shear-lag modified Halpin–Tsai scheme, it is necessary to divide the material into individual laminates that are later reassembled. The first assumption is that the fiber orientation is planar. The fibers are divided into laminates with the same fiber type. Since an individual fiber length assessment per fiber orientation class is not feasible, the average fiber length of the respective type is assumed for all fibers as a second assumption. These laminates are now again divided into laminates with the same fiber orientation. In each case, angle intervals of 9° are combined. The procedure is shown graphically in the Fig. 6. The stiffness properties of each UD layers is determined using the shear lag modified Halpin–Tsai method. A volume average of all laminates is calculated using formulations from the classical
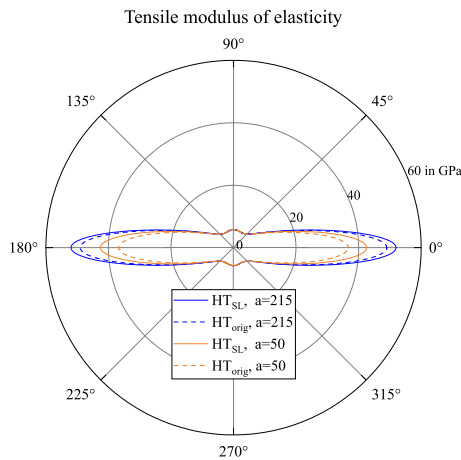
Fig. 5. Comparison of the original (orig.) Halpin–Tsai scheme with the shear-lag (SL) modified Halpin–Tsai scheme for different aspect ratios *a*.
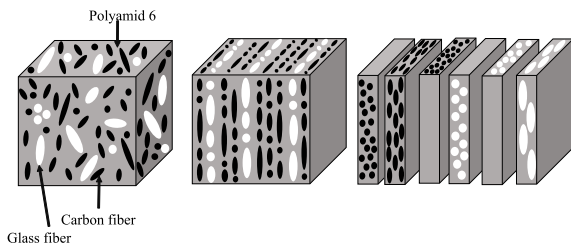

Fig. 6. Graphic representation in accordance with Yan [22] of the simplification of the hybrid into a planar distribution of the fibers and division into individual laminates with the same fiber type, the same fiber orientation and the average fiber length.

Table 2

Results of fiber weight and of fiber volume content from wet chemical removement.

Material Region	$F_{m.}$ in %	$F_{vol.}$ in %
CF_{LFT} (C)	32.90	23.6
CF_{LFT} (C-F)	33.89	24.4
CF_{LFT} (F)	31.84	22.7
CF_{LFT} (Average)	32.88	23.5
GF_{LFT} (C)	37.96	22.8
GF_{LFT} (C-F)	42.08	24.89
GF_{LFT} (F)	43.91	26.3
GF_{LFT} (Average)	41.31	24.66
$CF + GF_{LFT}$ (C)	31.31	19.37
$CF + GF_{LFT}$ (C-F)	31.67	19.59
$CF + GF_{LFT}$ (F)	32.70	20.23
$CF + GF_{LFT}$ (Average)	31.89	19.73

Table 3

Results of fiber length distribution.

Material Region	L_p in mm	L_n in mm	Median in mm
CF_{LFT} (C)	5.9	1.45	0.50
CF_{LFT} (C-F)	7.57	1.45	0.50
CF_{LFT} (F)	5.68	1.77	0.77
CF_{LFT} (All)	6.38	1.55	0.54
GF_{LFT} (C)	5.38	1.45	0.62
GF_{LFT} (C-F)	5.40	1.13	0.49
GF_{LFT} (F)	3.93	0.97	0.52
GF_{LFT} (All)	4.90	1.18	0.53
$CF + GF_{LFT}$ (C)	7.97	1.71	0.56
$CF + GF_{LFT}$ (C-F)	6.83	1.85	0.79
$CF + GF_{LFT}$ (F)	7.24	2.09	0.75
$CF + GF_{LFT}$ (All)	13.6	1.86	0.68

laminate theory. The synthetic thickness of the laminate is determined by the percentage of fibers with an angle in the corresponding range. This scheme is explained in more detail in [20], where it is called LAA.

3. Results and discussion

This chapter presents the Results of microstructural investigations, macroscopic characterization of effective mechanical properties, and the two homogenization methods. These results are thoroughly discussed and compared to validate their accuracy. Moreover, the effect of hybridization in mixed fibers in reinforced LFT is discussed.

3.1. Fiber volume content distribution

The fiber volume content (FVC) of all material types separated into the three extraction areas and as average, are shown in the Table 2 below. It can be seen that the desired volume percentages of 25% were achieved quite well with the single-fiber materials (CF and GF). In the case of CF_{LFT}, the average FVC was lower by 1.5% and for the GF_{LFT} by 0.34%. This shows that the accumulation of the desired volume content for the individual fibers works very reliably. The hybrid shows that the fiber volume content was significantly underestimated and is only approx. 20%. This is due to the fact, that in the calculation table used during the manufacturing process, the fiber content is only referenced to the polymer stream, which led to an error in the insight calculation. The lower volume fraction of the hybrid must be taken into account in the assessment of the mechanical properties.

Significant differences in FVC could be observed between some samples. These variations in fiber volume content across the plate are typical of LFT materials and can be seen in all materials. In the case

of specimens with a particularly high FVC, this could be attributed to the presence of fiber bundles on the basis of the CT data. In the case of GF-LFT the fibers appear to be increasingly entrained by the polymer flow, so that lower fiber contents were determined in the charge area. Since only one plate was examined this could also be a random effect. Overall, however, no significant influence of the different removal areas on the FVC could be detected, so a homogeneous distribution of the FVC over the whole plate is assumed with the average value for the later homogenization.

3.2. Fiber length distribution

Table 3 shows the results of the fiber length measurements of the individual materials divided into the three extraction areas. The number average value L_n and weight average value L_p as well as the median are given.

The values in the table show that the fiber lengths differ significantly between the two mono fiber materials. The CF seem to suffer less damage in the extrusion process than GF and are longer in the finished parts. The reason for this could be, that the CF rovings, due to their lower density and higher tex, contain many more fibers, which make separation and fiber breakage more difficult. In the hybrid material, the fibers are present the longest on average over both fiber types. Thus, it could be that the different fiber types positively influence each other through their interaction in the TSE, resulting in lower damage which itself results in longer fibers in the plate. However, due to the lower fiber volume, it cannot be ruled out that also the lower content is responsible for the lower fiber shortening. Despite the low average fiber lengths of all the materials, they are still referred to as LFT materials because this description is not just about fiber length, but is a general process description.
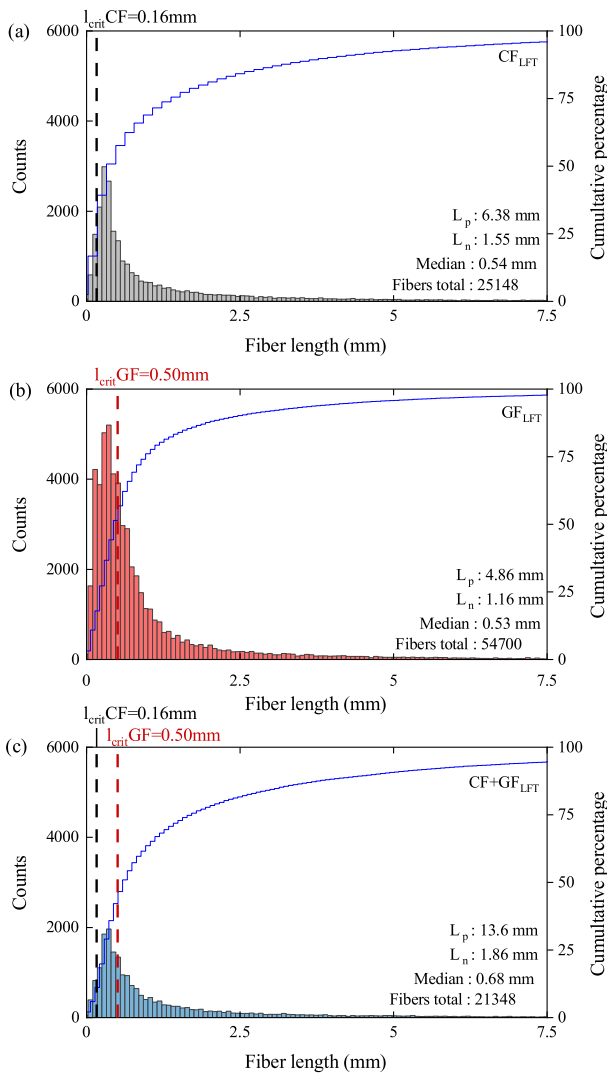
Fig. 7. Fiber length distribution of all 9 specimens together divided into categories with a width of 75 μm (a) CF_{LFT}, (b) GF_{LFT} and (c) $CF + GF_{LFT}$.

Table 4
Aspect ratio homogenization.

Material	Diameter in μm	Aspect ratio
CF_{LFT}	7.2	215
GF_{LFT}	16	73
$CF + GF_{LFT}$ (CF)	7.2	258
$CF + GF_{LFT}$ (GF)	16	116

For the homogenization section, L_n, the mean fiber length of all measured fibers is used for the determination of the aspect ratio. This leads to a aspect ratio of the mono fiber and the fiber blend material given in Table 4. These aspect ratios are used for the subsequent homogenization.

3.3. Microstructure and fiber orientation

In this section, the results of the microstructure investigations based on micrographs and micro CT data are presented and discussed. In particular, the differences between the various fiber compositions are discussed. The μCT data are analyzed, discussed and given with regard to the necessary formats of the fiber orientation for the different modeling approaches.

3.3.1. Micrograph based analysis

The Fig. 8 shows micrographs of the hybrid from both areas with viewing plane perpendicular to the flow front. The micrographs of the hybrid material are shown here, as these images are the best way to assess the fiber dispersion of the individual fiber types in the hybrid. Since the images were taken under a reflected-light microscope, the CFs appear white because they reflect the light, while the GFs, which are translucent, appear gray. The individual fiber type can also be identified by the different diameters of the fibers. The fibers can be seen simplified as round cylinders, whereby the orientation of the fiber can be determined from the ellipse created by the cut of the fiber through the method of ellipsoid. The micrographs of all materials generally show a different microstructure in the charge and flow area. In the charge area (Fig. 8(b)), fibers can be seen in the edge layers, whose sectional surface forms a very elongated ellipse. From this it can be seen that the fibers lie in the cutting plane and thus close to the 90° to the flow front. Due to the extrusion process, the fibers in the initial charge are present in the outer layers in the extrusion direction. This effect was demonstrated by Schreyer et al. by investigating the fiber orientation in the initial charge of CF_{LFT} (cf. Fig. 8 (a)) [69]. This layer freezes directly during the molding process and can also be seen on the surface in the later sheets. Since the molding process was selected in such a way that the flow direction is 90° to the extrusion direction(cf. Figs. 3 and 8(a)), it can be concluded that the fibers in the edge areas of the micrographs are remnants of the edge layer of the initial charge. In the inner core area of the charge area (Fig. 8(b)), most of the fibers are cut that a very round ellipse is created and thus point out of the cutting plane. This means they are aligned close to the direction of the flow (0°). In the core area, only a partial dispersion of the fibers is visible. The individual fibers are well impregnated and surrounded by matrix, but appear more in clusters of CF and GF. No shell core effect can be detected in the flow area, the fibers are aligned in flow direction up to the edge(Fig. 8(a)). In itself, the structure is very similar to the core from the charge area (a), the fibers seem to be well impregnated individually, but they also appear in clusters or bundles of the fiber types. A similar behavior can also be observed with the mono fiber materials. To get a better overall impression of the microstructure, Fig. 9 shows the complete micrographs of a 12 mm ×12mm sample from the flow area of all three materials. The microstructure of the CF_{LFT} (Fig. 9(a)) and GF_{LFT} (Fig. 9(b)) mono fiber materials is clearly distinguishable from one another by their micrographs. The glass fibers are usually surrounded to a large extent by matrix. When they occur

Graphs of the fiber length distribution for the overall average of all specimen of the CF_{LFT} (a), GF_{LFT} (b) and the $CF + GF_{LFT}$ (c) is shown in Fig. 7. The fibers are displayed in a histogram divided into categories with a width of 75 μm. The exact number of fibers measured and the characteristic values from the table are noted in each graph. In addition, the critical fiber length l_{crit} calculated according to the Eq. (2) (with the values given in Section 2.2.1) is indicated at 0.16 mm by a black vertical line for the CF and at 0.50 mm by a red vertical line for the GF.

At first glance, the graphs of all three materials look very similar and a large proportion of the fibers are in the range of 0 mm - 1.25 mm. Nevertheless, the shape of the distribution curve is as expected for fiber-plastic masses processed in an extrusion process. However, if the l_{crit} in the mono fiber materials is taken into account, it is noticeable that for the CF a large proportion of the fibers (approx. 80%) exceed l_{crit}, while for the GF only about half (approx. 50%) of the fibers exceed l_{crit}. Since it was unfortunately not possible to determine the fiber lengths in the hybrid individually, only the mixed spectrum can be considered for the hybrid. Due to the average length of the fibers, which is even longer than in the CF_{LFT}, and the significantly higher number of CF due to their smaller diameter, it can be assumed that the majority of the fibers exceed l_{crit} here as well.
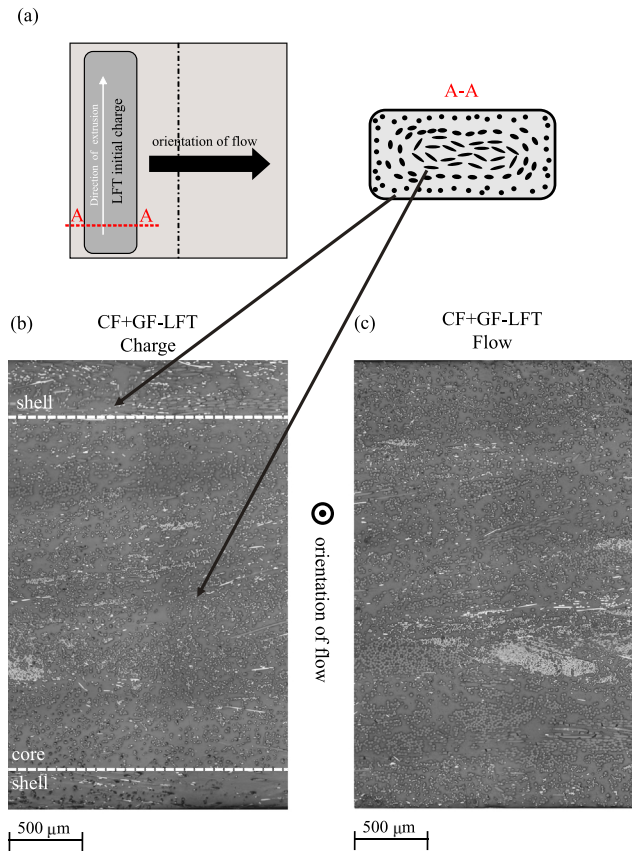
Fig. 8. (a) Schematic cross section of the initial charge and micrographs of the hybrid of charge and flow area, with the typical shell core structure, in white the CF and in gray the GF. In (b) Charge area with the characteristic frozen fibers in the structure of the initial charge 90° to the flow direction in the shell and the fibers aligned in 0° in the core. (c) Flow area with less fibers in the shell and more bundles in the core in both areas with main orientation to the flow direction.

Fig. 9. Micrographs with a representative microstructure of flow area of (a) CF_{LFT}, (b) GF_{LFT} and (c) the $CF + GF_{LFT}$ with high amount of CF-Bundles.

in bundles, these are usually bundles with a very small number of fibers, in which the fibers still seem to be well impregnated. The CF in the hybrid and mono-fiber material, on the other hand, show good impregnation in areas where there are few fibers. However, they occur more frequently in bundles consisting of a large number of fibers, which leads to poor impregnation in some cases. In a few cases, there are even bundles with un-impregnated fibers inside. These un-impregnated areas can be recognized by the black holes, since the un-impregnated fibers are pulled out during the grinding process. The micrographs of the hybrid LFT Fig. 9(c) show that the material consists mostly of large areas where the fibers are still present in clusters of their own fiber type or even in bundles. It is noticeable that the formation of bundles is mostly observed with the C-fiber. This can be attributed to the fact that, due to the lower density, the lower diameter and the higher tex number of the roving, significantly more CF are present in the hybrid LFTs. As noted in Section 3.1, it is likely that the unraveling of the CF-Rovings and the impregnation of the fibers will take more time and effort than with the GF. Comparing the fiber distribution in the hybrid with that of the mono-fiber materials in the figure, it is noticeable that the fiber types themselves differ, but behave similarly in both cases. All in all, it is noticeable that the GF seem to be easier to cut and distribute due to their smaller number. However, the results from the fiber length distribution (cf. Sec., 2.2.1) seem to indicate that this is also accompanied by increased fiber shortening. The CF fibers, on the other hand, remain partially clumped and the bundles are not completely dissolved.
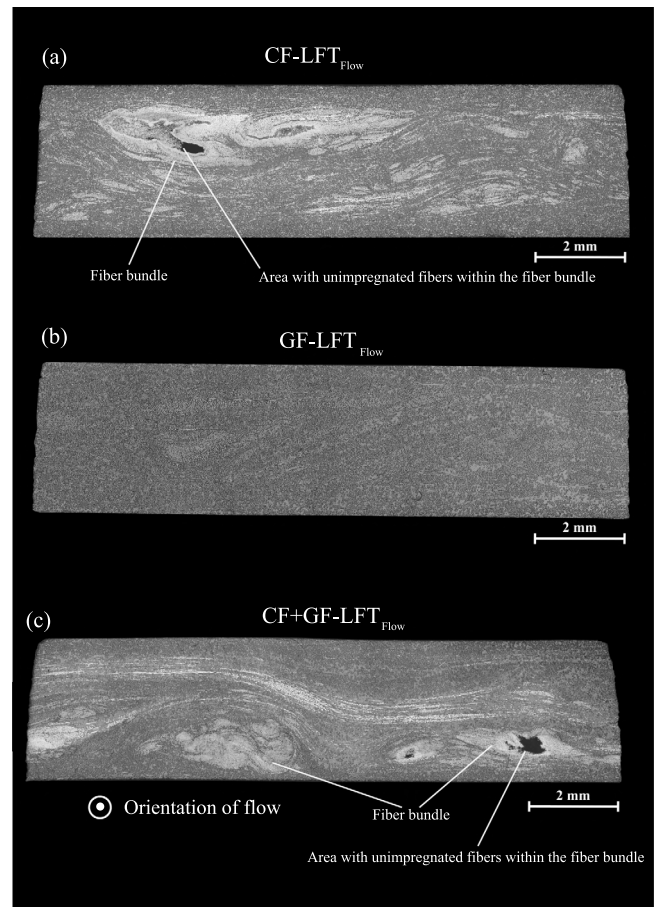
3.3.2. μCT based analysis

An example slice of the CT scan of the center specimen CF2 of all three plates can be seen in the first row of Fig. 11. Regarding the CF reinforced specimen Fig. 11(a), the image is more noisy and the fibers are more difficult to detect due to their smaller diameter compared to GF, even though the resolution is a bit higher for the CF and the hybrid plate. The hybrid plate shows the bundle formation of the carbon fibers very well as they are detectable as big darker spots in the image. When visualizing the detected orientations of the structure tensor code in pseudocolor image (cf. Fig. 11(b)), the disadvantage of the worse image quality in the GF_{LFT}(CF) picture is revealed. The orientation seems to be a bit patchy and in addition, it is not clear whether all single fibers are detected, which could lead to a overestimation of the bundle orientation. The glass fibers are well-identified in the single fiber reinforced plate (GF_{LFT}(GF)) as well as in the hybrid ($CF + GF_{LFT}$(GF)). As the gray value of the carbon fibers is so close to the matrix due to their similar density (both are mainly carbon atoms) and therefore the contrast in the image is low, they are hard to recognize in the slice of the hybrid sample ($CF + GF_{LFT}$(CF)). It cannot be excluded that parts of the matrix are included in the evaluation of the carbon fiber orientation of the hybrid sample.

The result of tensor interpolation was presented in the form of fields of tensor glyphs. The plots were made with the help of the Matlab fanDTasia ToolBox from Barmpoutis for the visualization of higher order tensors [70]. The result can be seen in the left column of Fig. 10. The second column displays one single tensor glyph representing the overall averaged tensor of a plate, which is also the tensor that was used in the Mori–Tanaka homogenization. The right column shows the
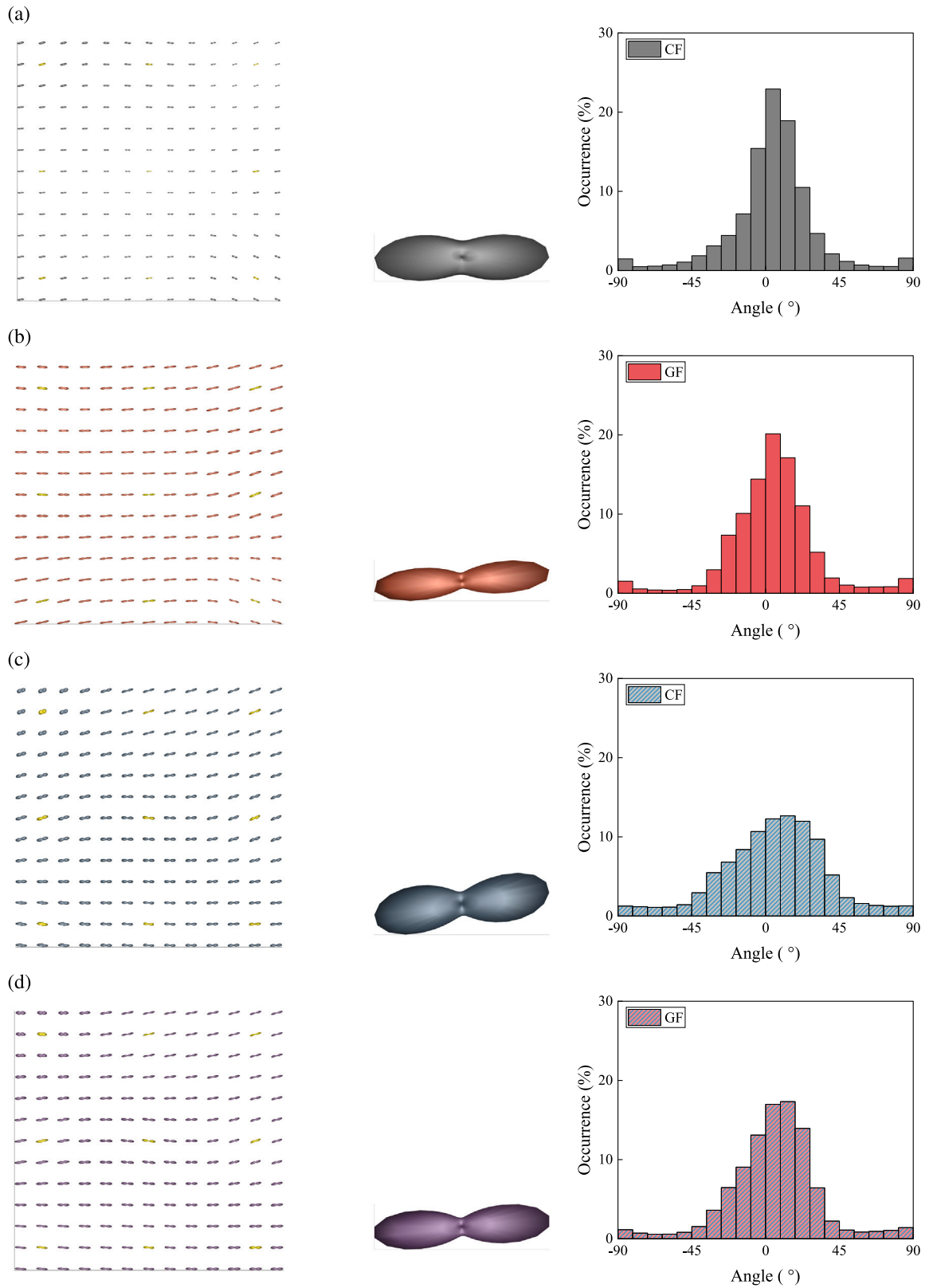
Fig. 10. Field of tensors of fourth order, averaged tensor glyph of all 169 tensors of fourth order and histogram of orientation distribution of the mean of all specimen in degrees for 20 groups (width of one column: 180°/20), for the CF plate (a), the GF plate (b), the carbon fibers in the hybrid plate (c) and the glass fibers in the hybrid plate (d).

fiber orientation distribution histogram as the mean of all 9 specimen for 20 groups with an interval arc length of $\pi/20$, which was the basis for the Halpin–Tsai homogenization. It is clearly visible that there is tendency towards an upwards drift at the right side of the plate. This

fact is already known from earlier publications [13,25,30,71]. The authors assume that this is related to the "age" of the initial charge. The part that left the nozzle early and was therefore in the air longer behaves differently than the other end. This was confirmed by reversing
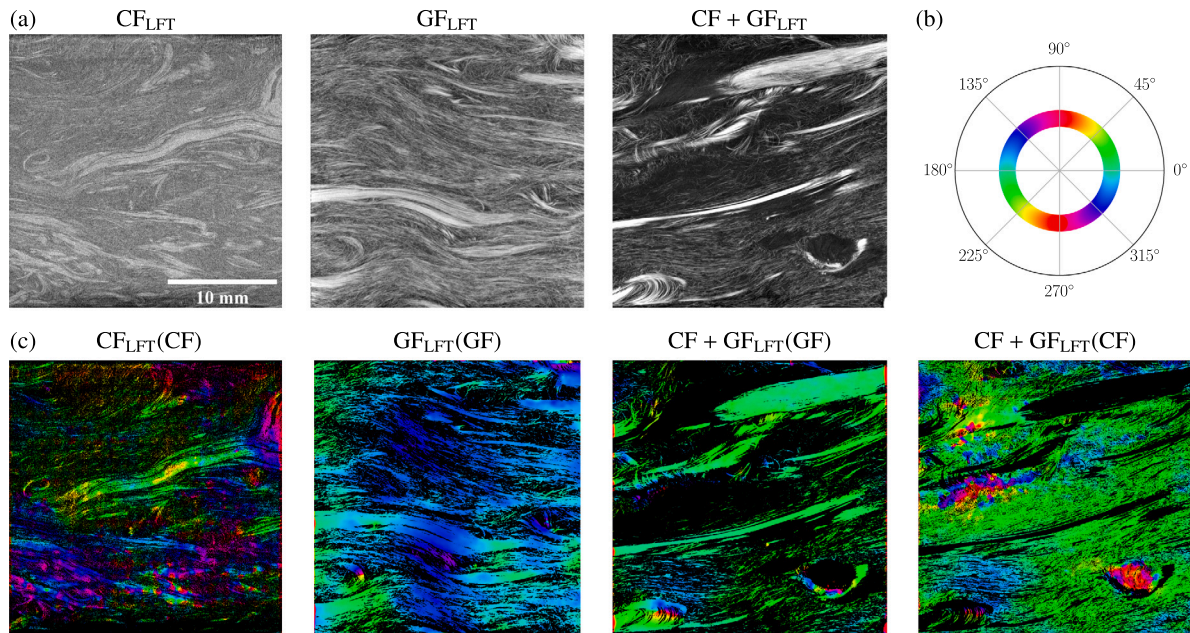
Fig. 11. (a) One slice out of the middle of the CT scan of the CF2 stack of the CF reinforced plate, of the CF2 stack of the GF reinforced plate and of the hybrid CF+GF reinforced plate. (b): Color-angle correlation in the HSV ("Hue Value Saturation") color space. (c): Detected fiber orientations in the slice presented in (a) through the code by Pinter et al. [33] visualized in the HSV color space. For the hybrid CF+GF reinforced plate separate visualizations of the detected fiber orientation for GF and CF.

the insertion of the initial charge, which in contrast led to a downward drift. Furthermore, the averaged tensor glyph of the CF plate appears to be a bit rounder than the averaged tensor glyph of the GF plate. This is valid for both the purely carbon fiber reinforced plate as well as for the hybrid plate. This finding is confirmed when considering the histograms. The histogram is flatter and wider for the CF part and more narrow and pointy for the GF plate. This appears reasonable because the fiber orientation pattern was generally much more confused and developed in different directions in the case of carbon fibers. Overall, the resulting orientation when only averaging the nine measured tensors were compared with the resulting orientation when averaging all measured and interpolated ones of a plate, with the latter being closer to the experimental results. This is due to the fact that the information of a measured tensor is very local. By the interpolation rather a global orientation behavior of the plate is represented, which therefore fits better to the averaged experimental values of a plate. Consequently, the authors use the interpolation method and average all 169 tensors before passing them on to the modeling.

3.4. Tensile tests

In Fig. 12, for all materials and separated into charge and flow area, the tensile modulus of elasticity (a) and the tensile strength (b) curves in the polar plot are given as a function of the angle relative to the flow (as shown in Fig. 3(e)). Each measuring point (with orientations 0°, ±11,25°, ±22,5°, ±45° and 90°) consisting of at least five valid samples and is shown as mean value with the standard deviation. In order to better relate the individual measurement points of a category to each other, they were each provided with a linear connection.

In all three material combinations, the 0° orientation to the flow path shows the highest reinforcement effect of the fibers in case of tensile modulus and tensile strength, while the 90° orientation shows the lowest. While the mechanical properties remain almost unchanged at small angles deviating from 0° (+11.25°), there is already a significant drop at somewhat larger angles (+22.5°). At an angle of +45°, another significantly stronger drop can be seen. The characteristic values here are very similar to those at 90°, which show the minimum.

This behavior indicates a strong orientation of the fibers in the direction of the flow front. It is striking that no significant difference

can be detected between the charge and flow areas of the individual materials. This means that there must also be a strong orientation of the fiber in the charge area.

This effect can be confirmed by the micrographs and the analysis of the CT data from chapter 2.2.3 and chapter 3.3.1 in which an alignment in the direction of the flow is detected in both the flow and the charge area. Since the shell structure in the charge area with the fibers in the 90° direction to the flow (cf. Section 3.3.1, Fig. 8)only takes up a small part of the volume, it has no great influence in the tensile test. In bending tests, the influence of this layer is greater due to the uneven stress distribution, which was already demonstrated by Schelleis et al. [25].

It can also be clearly seen that the curves are not symmetrical to the 0°–180° orientation line, but a rotation towards the positive degree counts (upwards) can be seen for all three materials. This is visible in both, the tensile modulus and the tensile strength. The strength and stiffness values at +11.25° and +22.5° are clearly higher than those at −11.25° and −22.5°. Since the CF shows the most significant reinforcement effect due to its high stiffness and high strength, this effect can be most clearly illustrated by the CF$_{LFT}$. While the values of 0° (23.83 GPa) and +11.25° (23.82 GPa) remain almost the same, a drop of approx. 30% can be observed between 0° and −11.25° (16.71 GPa). This suggests that the main orientation of the fibers in the molding process is between 0° and +11.25° due to an inclined flow front. For the hybrid and the GF-LFT, the stiffness values in 0° and +11.25° are also equal, while there is a significant drop from 0° to −11.25°. A similar effect was also shown by Bondy et al. who demonstrated a difference in the mechanical properties of CF$_{LFT}$ between ±45° [13]. Schelleis et al. were also able to show a similar effect with glass fiber reinforced polycarbonate from the LFT-D process on the basis of different material properties [25]. Fliegener was also able to show a drift for GF-PA6-LFT based on the determination of fiber orientation tensors by μ CT [71]. Since, as mentioned in , the drift is in the opposite direction when the initial charge is rotated 180°, the effect must come from the initial charge it self. Reasons for the development of this inclined flow front could be temperature gradient or geometric differences in the initial charge. Since the beginning of the initial charge has been out of the extruder for a longer time, more cooling can occur there. The outer layer of the initial charge cools to 210°, where solidification begins.
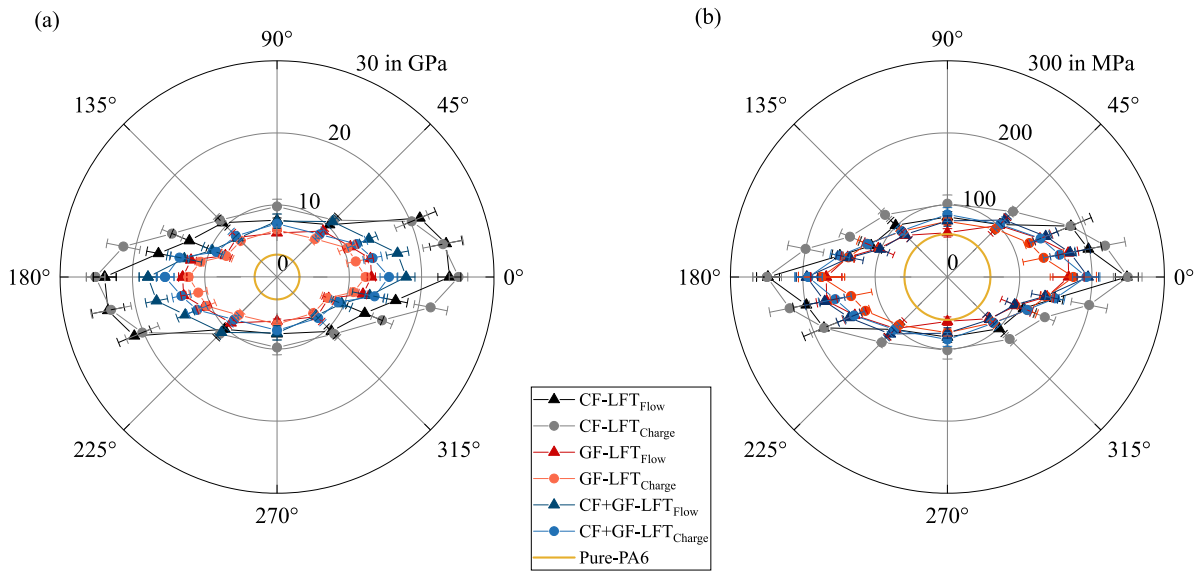
Fig. 12. Polar diagram of (a) tensile modulus of elasticity and (b) tensile strength of the three different LFT-Materials in different orientation to the flow direction separated by charge and flow area.
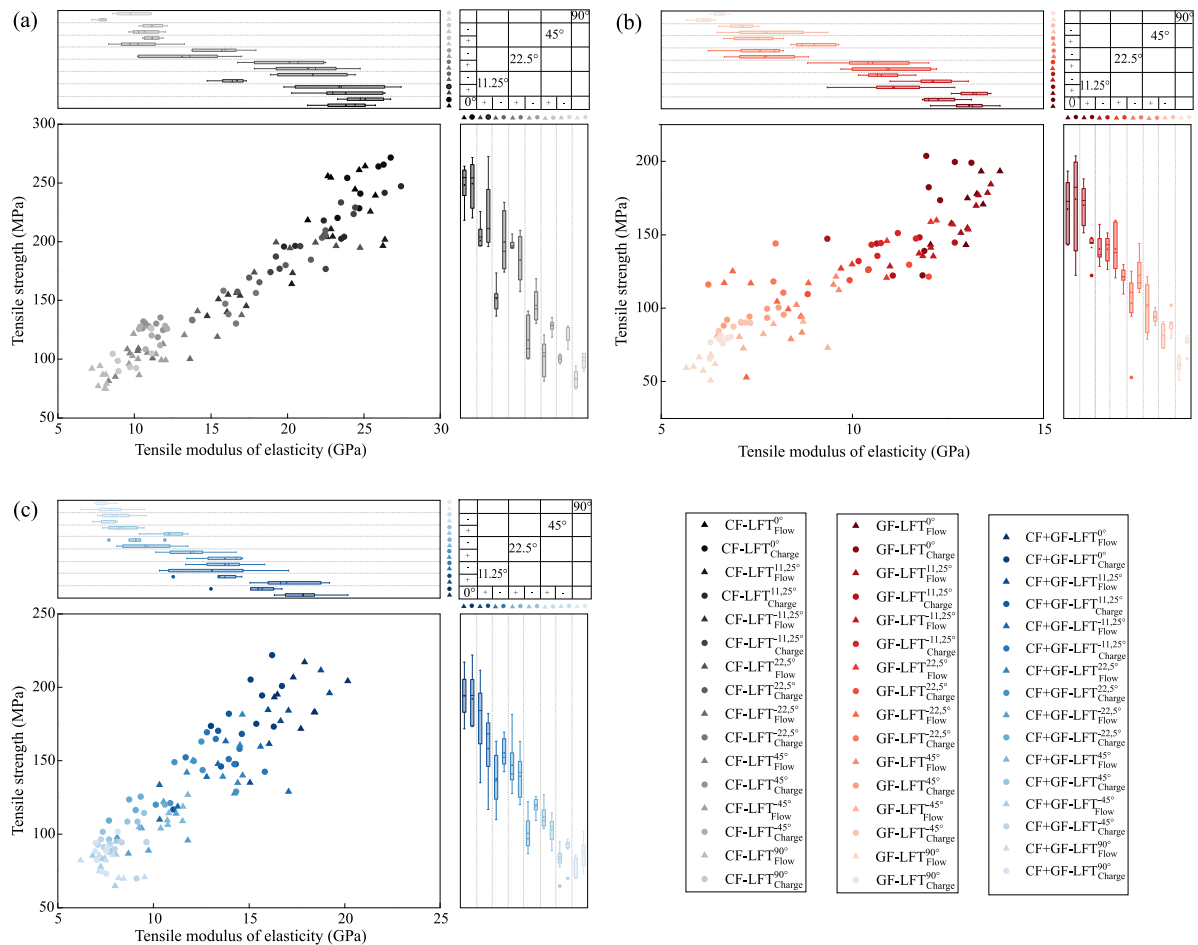

Fig. 13. Tensile strength over tensile modulus of elasticity of (a) CF_{LFT}, (b) GF_{LFT} and (c) $CF+GF_{LFT}$ each separated by the triangle symbol in Flow and by the dot symbol in Charge area. The individual orientations are symbolized by the different brightness gradients, where dark indicates the 0° and the bright the 90° orientation.

This layer must be broken up during the pressing process to allow the plasticized interior to flow into the mold. If this layer is thicker at the old end of the initial charge than at the new end, it will be broken first at the new end and the interior will flow out there first. A schematic representation of a possible temperature distribution in the initial charge is given in Fig. 14(a) This can also be seen from the mold filling study in Fig. 14(b)–(g), which shows that the mold is initially filled only in the lower left corner. As a result, an inclined flow front develops
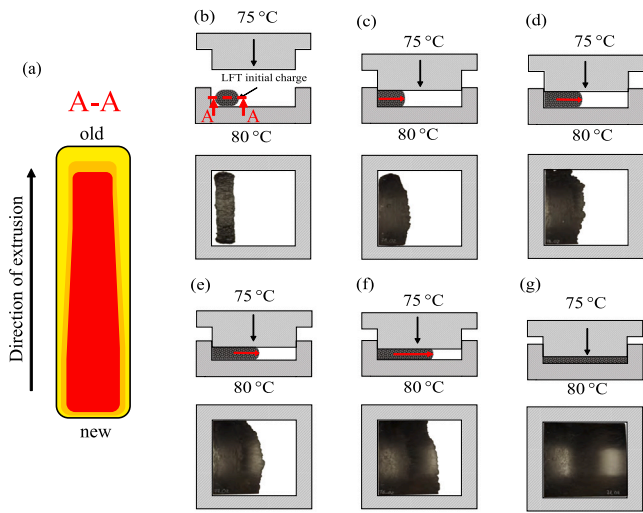
Fig. 14. Mold filling study of the compression molding of CF_{LFT} (a) a possible temperature distribution in the initial charge with young and old end (b) - (g) compression molding process with development of the flow front and mold filling.

Fig. 15. Linear regression in tensile strength versus elastic modulus diagram between all tensile tests independent of orientation and position of CF_{LFT}, GF_{LFT} and $CF + GF_{LFT}$.

Fig. 16. Effect of hybridization on the example of specimen from the flow area in 0° orientation to the flow front, were the highest reinforcement effect of the fibers could be observed.

throughout the process, which also affects the fiber orientation and thus the mechanical properties. From the geometric side it could be possible the first part of the initial charge will be stretched by falling onto the transport belt. This could result in less material at the old end of the initial charge. At the same time, there is a deformation of the initial charge at the end caused by the cutting process. This could lead to an excess volume at the end of the initial charge. Thus, during pressing, the uneven distribution of material results in an excess volume in the lower part of the mold, which leads to a slanted flow front directed upwards, since there is less volume there.

The fact that all materials show a strong decrease in mechanical properties at small angles away from the maximum between 0° and 11.25°, indicates a strong alignment of the fibers. In addition, it can be seen that both in 0° and in 90° orientation, the CF_{LFT} shows the highest tensile strength and stiffness of all materials, which indicates the trend towards CF-DiCo-FRP. In order to show the experimental results from the tensile test in more detail, each test is shown as a measuring point in the tensile strength versus tensile modulus of elasticity diagram in Fig. 13 (divided into one diagram per material (a) CF_{LFT}, (b)GF_{LFT} and (c) $CF + GF_{LFT}$). Again, samples from the charge area are shown as points and from the yield area as triangles. To distinguish the individual orientations, a different color was chosen for each orientation. In addition, boxplots for tensile strength and tensile modulus of elasticity are given at the edge. The box plots again show the clear difference between the + and — orientation, especially at small angles (±11.25° and ±22.5°). The scattering areas hardly overlap,so a significant effect can be assumed for all materials.

Furthermore, it is noticeable that tensile strength and tensile modulus of elasticity viously show a linear dependence per material. Looking at the results of all orientations from both areas in the tensile strength versus tensile modulus diagram, a linear correlation of the values can be seen for all three materials with a certain scatter. For this purpose, a linear regression was performed between all values of a material in Fig. 15. The GF_{LFT} regression line shows the highest slope and therefore the lowest stiffness-to-strength ratio, while the CF_{LFT} regression line shows the lowest slope and therefore the highest ratio. This illustrates that the use of CF in the LFT process mainly provides a significant increase in stiffness and is therefore suitable for stiff components. Of course, this is due to the properties of the fibers themselves, as their higher stiffness when oriented close to the main fiber orientation naturally causes a stronger stiffening effect, which in turn affects the pitch. The straight regression of the hybrid is pretty much between the
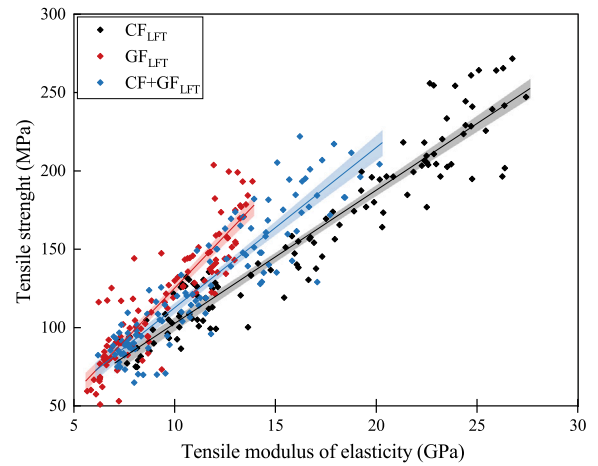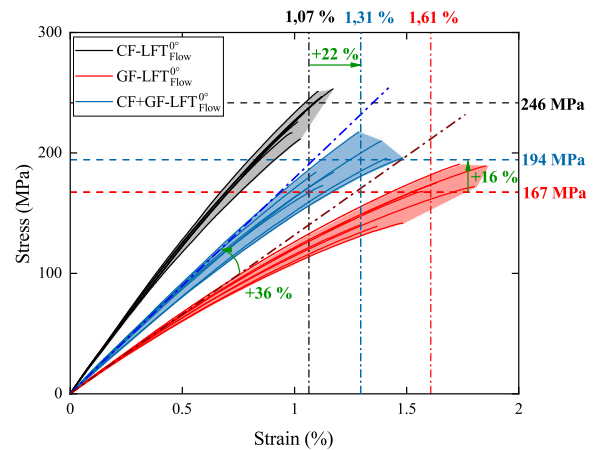
two monofiber materials. Since the hybrid consists of equal parts of the two fibers, this is not surprising. It can be assumed that for blends with a higher proportion of GF, the slope of the regression line will be shifted more in the GF_{LFT} direction and with CF in the CF_{LFT} direction.

3.5. Effect of hybridization on mechanical properties

As can be seen in Fig. 12 based on the stiffness and strength of the materials, between the 0° and +11.25° orientation, the largest reinforcement effect due to the fibers and thus also the greatest difference can be seen for all three materials. For a comparison and evaluation of hybridization effects, one of these type of samples are best suited. Therefore, the stress–strain curves of all tested specimens with 0° orientation from the flow range are shown in Fig. 16. In addition, the scattering range is marked by the colored background. It can be seen clearly, that the curves of the hybrid are between the two materials reinforced with only one type of fiber. The colored areas clearly show that the results in the test are subject to considerable scattering, but there is no overlapping of the individual areas. Therefore, the hybridization effect in this case is presented on the basis of the mean values of the specimen type of the individual material systems. The positive hybridization effect after definition (a) in Fig. 2 is now shown by the green arrows. The hybrid shows a 16% increase in tensile strength and a 36% increase in the tensile modulus of elasticity compared to

Table 5

Mechanical characteristics and production values of hybrid-LFT in comparison to GF- and CF-LFT.

Parameter	Hybrid/ GF_{LFT} in%	Hybrid/ CF_{LFT} in%
Tensile strength in 0°	116	78
Tensile Modulus of elasticity in 0°	138	75
Elongation at break in 0°	81	122
Weight	91	104
Price primary Fibers	177	64
CO_2 primary Fibers	162	69
Modulus per weight	152	72
Modulus per price	78	117
Modulus per CO_2	85	109

Table 6

Rule of Mixture of 0° Flow Specimen.

Parameter	RoM	adj. RoM	Exp.
σ_m in MPa	207.85	180	194.4
$E_{tensile}$ in GPa	18.4	15.43	17.9

Fig. 17. Results of modeling with HT and MT based on determined fiber orientation via μCT.

GF_{LFT}. This is in a similar range to the results of Fu and Lauke et al. where an increase in the tensile modulus of elasticity of a hybrid of equal parts CF and GF causes an increase of about 33% compared to pure GF composite [6]. There are also examples in the literature that could determine a much stronger effect. Wollan, for example, was able to determine an increase of 106% comparing a hybrid of equal parts CF and GF with the pure GF-composite, both based on PA6 [72]. However, the production of the materials is not a direct process in which the fibers still have to be impregnated, but rather pre-impregnated pellets that already consist of both fiber types [72]. Therefore, a good impregnation of the fibers can be expected. This supports the hypothesis that the CF in the hybrid investigated in this work do not exploit their full potential because they occur in bundles.

In this work additionally a 22% increase in elongation at break compared to CF_{LFT} could be observed. It has already been demonstrated, that the interfacial shear stress reaches its highest value at the fiber ends [73]. Since the carbon fiber has a higher stiffness than the glass fiber, it can be assumed that the higher maximum value in terms of the stress transfer theory is found at the carbon fiber ends. It can be assumed that the first crack is also initiated at the here [21,73]. The cracks that form at the CF now grow through the matrix until they reach a GF that bridges them. Therefore, these cracks do not lead directly to failure. Failure is initiated when these cracks grow together with the cracks forming at the end of the GF [6]. A schematic representation of the micro failure process for CF+GF Dico materials can be found in Fu and Lauke et al. [6, p. 1250] and in Li et al. [21, p. 1729]. This shows that the hybrid mechanically combines the best properties of both materials.

A summary of the performance of the hybrid — LFT compared to the base of CF_{LFT} and GF_{LFT} is given in Table 5. From this, some promising combination options of mixed fiber LFT for different optimization targets can be identified. By adding CF in the GF_{LFT} it can be significantly improved in terms of weight specific modulus by 52%. The CF_{LFT} shows by the addition of GF in contrast a smal increase in the price an CO2 specific modulus. Since the hybrid investigated in this work fitted perfect between the GF_{LFT} and the CF_{LFT}.

Table 6 gives the experimental results of the hybrid calculated using the RoM Eq. (1). Since the fiber volume content in the hybrid is significantly lower than in the two monofiber materials, an adapted RoM was also used in which the lower volume content of 20% is realized by an extra proportion of pure matrix. This can be achieved with 40% each of GF_{LFT} and CF_{LFT} and additionally with 20% pure matrix to $E_{hybrid} = 0.4 \cdot E_{GF-LFT} + 0.4 \cdot E_{CF-LFT} + 0.2 \cdot E_{PA6}$. The results with the adjusted RoM: are also given in Table 6. As can be seen, the experimentally determined values are slightly below the RoM. The hybrid misses the RoM by only 7% with respect to σ_m and by only 3% with respect to $E_{tensile}$. Especially with regard to $E_{tensile}$, the RoM shows a good over coordination when considering the scatter of the measured values, but according to definition b) no positive hybridization effect.
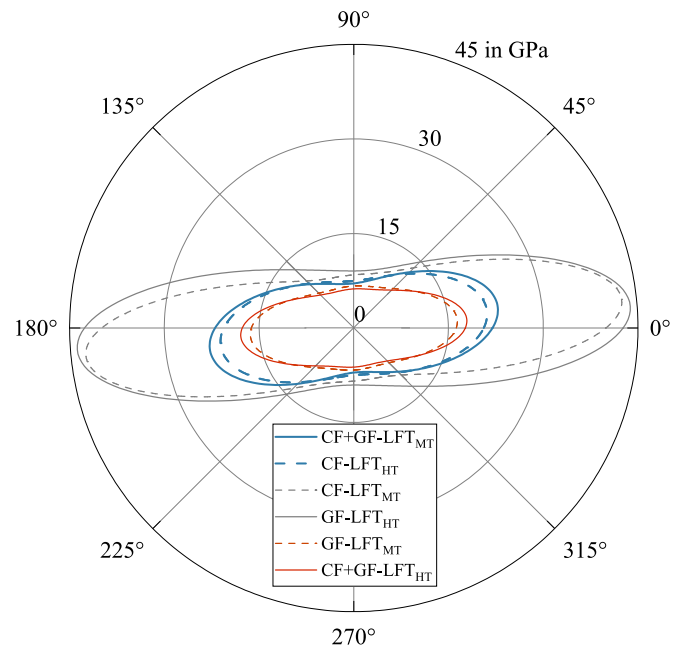
In contrast, the adjusted RoM is outperformed by the hybrid in terms of σ_m by 8%, which is exactly between the two estimates. In terms of $E_{tensile}$, the hybrid outperforms the adjusted RoM by 16%. This illustrates that hybridization has a stronger influence on stiffness than on strength. If we now take the adj. RoM in as reference, the hybrid shows a positive hybridization effect according to definition b).

Almost putting the two definitions of the effect of hybridization together, it can be said that according to definition a, a positive effect is visible, according to b it depends on whether you consider the normal RoM or the adjusted RoM.

3.6. Homogenization

The results for the homogenization procedure by using the MT scheme and HT scheme are given in Fig. 17. It can be seen that the prediction of the pure carbon fiber reinforcement achieves the greatest stiffening effect, thus enclosing the stiffness values of the hybrid and the glass fiber reinforced plastic at all angles. The hybrid completely encloses the pure glass fiber reinforcement, indicating a positive hybridization effect when carbon fibers are added to a glass fiber composite. This applies to both MT and HT homogenization. Furthermore, a preferred orientation of the stiffness can be seen, which does not coincide with the 0° direction, though. A slight drift in the direction of positive angles of about 8°–11° can be seen for all material systems. This drift numerically depends solely on the values of the orientation tensors used and is independent of the homogenization processes. A comparison with the experimental results of the stiffnesses suggests a correct measurement of the orientations of all material systems. The physical reasons that could be responsible for this drift have already been discussed in Section 3.4.

Individual comparisons of experimental and numerical results for each material system are displayed in Fig. 18. Fig. 18a) compares
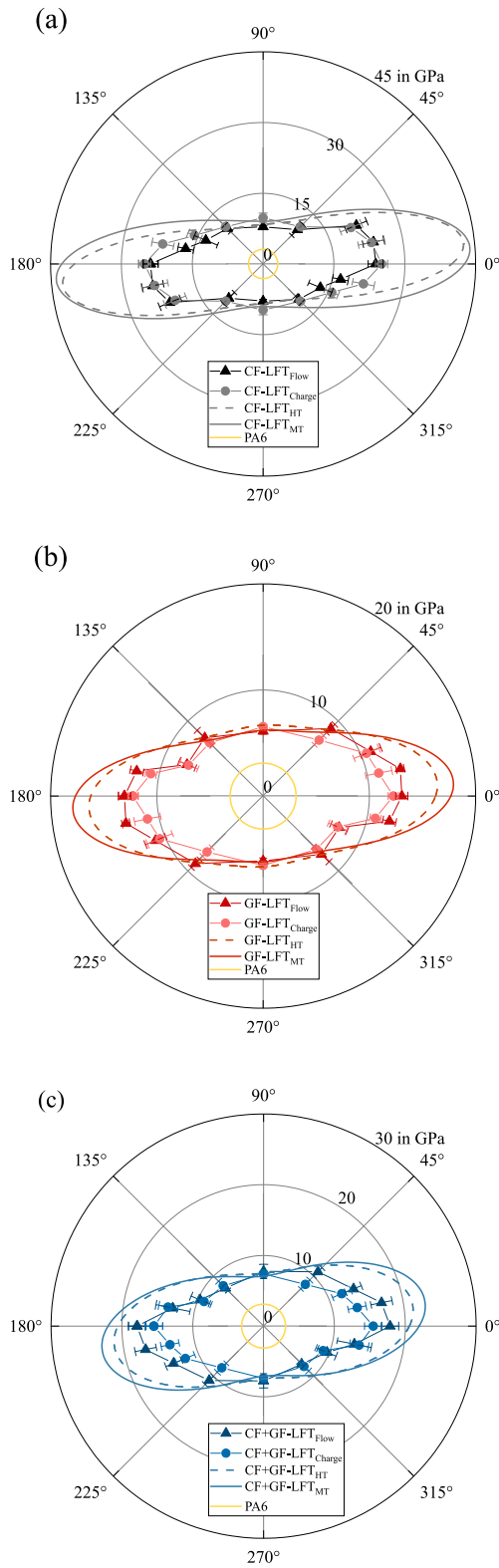
Fig. 18. Results of homogenization with HT and MT based on the determined aspect ratio (cf. 3.1) and fiber orientation via μCT (cf.)in comparison with the experimental results fore (a) CF_{LFT}, (b) GF_{LFT} and (c) $CF+GF_{LFT}$.

the experimental findings in discontinuously carbon fiber reinforced PA6 and the numerical results from the MT and HT homogenization schemes. The preferred orientation matches, which indicates a reasonable measurement and evaluation of fiber orientation, as described

in Section 3.3. The stiffness prediction in the orthogonal direction (i.e. the preferred direction $\pm90°$) agrees with the experimental findings for both MT and HT prediction. For the given fiber orientation measurements, the reinforcement effect is more pronounced in a small range around the preferred direction, since the first eigenvalue of the orientation tensor is close to one, indicating strongly aligned fibers. In this case, the fibers have a lower reinforcing effect in the $\pm90°$ direction. Nevertheless, the orthogonal stiffness significantly depends on the matrix properties. Matching stiffness values in this direction indicate a good assumption for the stiffness properties of the matrix material. The predicted stiffness values in the preferred direction ($8°$-$11°$) overestimate the experimental results by almost a factor of 2, with only minor differences between MT and HT. For both the MT and HT homogenization, the reinforcement effect increases greatly for an increasing fiber aspect ratio and fiber volume content. Possible explanations for this deviation between experimental and predicted results are given in the following. On one hand, the experimental measurements do not match the real values in the material and underestimate them. Considering the sensitivity of the used methods, this seems unlikely to create a deviation of this magnitude. Another, more likely explanation is that both homogenization procedures do not consider fiber interactions and assume evenly distributed, perfectly bonded fibers. As discussed in Section 3.1, the micrograph investigation indicates that the production process results in unevenly distributed fibers, which agglomerate in bundles. It can be assumed that fiber bundles have a reduced reinforcing effect in contrast to evenly distributed fibers. This is due to a weaker fiber–matrix bonding, up to the case of dry fibers, which do not reinforce the composite over all. Also fiber interactions within bundles is increased which also results in a lower reinforcement effect. As such, the measured fiber volume content and aspect ratio would need to be reduced to an effective value to respect these effects, when in reality the homogenization procedures do not respect these effects inherently. Fig. 18b) shows the differences in experimental and numerical results for the glass and carbon fiber reinforced hybrid. Again the orientations agree perfectly and the orthogonal direction once more indicates a good assumption for the matrix properties. The preferred direction is slightly overestimated with a better agreement for the HT homogenization scheme. The better agreement for the hybrid in contrast to the purely carbon fiber reinforced polymer in Fig. 18a) is explained by a better fiber distribution with less bundle agglomeration.

The pure glass fiber reinforced PA6 is displayed in Fig. 18c). This time, the predicted orientation is slightly overestimated for about $+3°$, while still achieving good stiffness agreements in the orthogonal direction. In comparison to the previous two material systems, the stiffness precitions are closest to the real experiment, with a slight overestimation once more. The HT homogenization has a slight better agreement with the experimental findings in comparison to the MT homogenization.

To conclude, both MT and HT give very similar stiffness predictions for planarly fiber reinforced polymers, with the MT prediction being slightly larger in magnitude in the preferred direction. In comparison to experimental findings the numerical predictions agree well, especially when the fiber orientation measurements are accurate. This also applies for the investigated hybrid material, indicating that stiffness properties of multi-inclusion FRPs can also be estimated with the investigated methods. It has to be emphasized that the numerical results do not agree well in the preferred direction for the solely carbon fiber reinforced polymer, which is explained by the fact that neither the MT nor HT scheme respect fiber bundle effects. A synthetic reduction of effective properties such as aspect ratio and/or volume content as a function of bundle content may alleviate the measured deviation.

4. Holistic discussion

In general, the determination of the fiber orientation by CT and post processing by interpolation and averaging shows a good agreement

with the experimental data. The drift of the main fiber orientation fits very well over each other in both methods. This allows a time efficient and accurate method of fiber orientation determination. By comparing both hybridization methods with the experimental results it could be shown that especially for CF_{LFT} such simple models are not sufficient to account for the influence of the complex microstructure. In order to achieve an adequate numerical description of the CF_{LFT} studied in this work, it is necessary to represent the microstructure more precisely. This can be achieved by a reduction of the aspect ratio due to the poor impregnation, especially of the long fibers in the bundles, as mentioned in Section 3.6. Another possibility is to reduce the fiber volume content for the calculation. Since the part of the fiber that is not impregnated or only slightly impregnated does not contribute to the load transfer.. A combination of reducing the aspect ratio and the fiber volume content is also conceivable. For this purpose, further analysis of the microstructure is necessary:

- CT data should be used to determine the probability of bundles in the volume.
- Micrographs should be used to determine the number and the degree of impregnation of the fibers in the bundle.
- Fiber length studies should be performed in which the bundles are separated from the remaining fibers after ashing and the fiber length of both parts is determined separately.

Furthermore, it is possible to use microstructure generators to create a representative volume element in which both dispersed and agglomerated fibers are represented in the correct ratio. For this purpose again, imaging techniques such as μCT data and micrographs provide a good starting point.

However, the further potential of CF_{LFT} with better distributed and impregnated fibers can be estimated based on the homogenization methods applied here. To achieve this, the use of rovings with a lower tex number would be recommended. This should lead to a faster fiber separation, resulting in fewer or at least smaller bundles in the structure. Another way to increase fiber dispersion is to apply higher shear forces to better separate the bundles. This can be achieved, for example, by an adapted screw geometry with more mixing elements or by higher screw speeds. It is expected that this will also result in greater fiber shortening. However, since a large fraction of the fibers are above l_{crit}, the fibers are likely to exceed l_{crit} by a large fraction even at higher shear forces. This and other process optimizations with regard to CF_{LFT} therefore offer a lot of potential.

For GF_{LFT} and $CF + GF_{LFT}$, where there is better dispersion of the fibers, the results are much closer to the experimental data. Therefore, it can be assumed that for well-distributed and impregnated fibers, the methods provide good results. On the basis of the experimental data it was shown, that the hybrid LFT of glass and carbon fibers can be described fairly accurate with the RoM. However, positive hybridization effects have also been demonstrated. In particular, the positive hybridization effect on the elongation at break of +22% compared to CF-LFT could indicate further potential. Since the GF limits the growth of cracks that form at the CF, this could also have a positive effect on fatigue properties. However, the combination of the two fibers opens up a large design space in which, depending on the requirements, the addition of CF in GF-LFT or vise versa can significantly improve the technical properties ore lead to a lower price and lower CO_2 emissions.

5. Conclusions

Overall, it has been demonstrated how mixed fiber composites can be experimentally investigated and numerically modeled. To the author's knowledge, this is the first time a Mori–Tanaka approach with two different inclusions has been used in a field study to ensure symmetric stiffness predictions following the method of Segura et al. In addition, the models for the first time are provided with fourth-order

plate-averaged orientation tensors that are both measured and interpolated. With well impregnated fibers in the materials, the mechanical properties can thus be well estimated. Thus, the design space between CF and GF can be predicted and estimated almost without gaps.

CRediT authorship contribution statement

Benedikt M. Scheuring: Writing – review & editing, Writing – original draft, Visualization, Validation, Software, Project administration, Methodology, Investigation, Formal analysis, Data curation, Conceptualization. **Nicolas Christ:** Writing – review & editing, Writing – original draft, Validation, Software, Methodology, Data curation. **Juliane Blarr:** Writing – review & editing, Writing – original draft, Validation, Software, Methodology, Data curation. **Wilfried V. Liebig:** Writing – review & editing, Supervision, Resources. **Jörg Hohe:** Writing – review & editing, Supervision, Resources. **John Montesano:** Writing – review & editing, Supervision, Resources, Conceptualization. **Kay A. Weidenmann:** Writing – review & editing, Supervision, Resources, Funding acquisition, Conceptualization.

Declaration of competing interest

The authors declare that they have no known competing financial interests or personal relationships that could have appeared to influence the work reported in this paper.

Data availability

Data will be made available on request.

Acknowledgments

References

[1] Böhlke T, Henning F, Hrymak AN, Kärger L, Weidenmann K, Wood JT. Continuous–discontinuous fiber-reinforced polymers: An integrated engineering approach. Carl Hanser Verlag GmbH Co KG; 2019.

[2] Ning H, Lu N, Hassen AA, Chawla K, Selim M, Pillay S. A review of long fibre thermoplastic (LFT) composites. Int Mater Rev 2019;65(3):164–88. http://dx.doi.org/10.1080/09506608.2019.1585004.

[3] Wan Y, Takahashi J. Development of carbon fiber-reinforced thermoplastics for mass-produced automotive applications in Japan. J Compos Sci 2021;5(3):86. http://dx.doi.org/10.3390/jcs5030086.

[4] Rajak DK, Pagar DD, Menezes PL, Linul E. Fiber-reinforced polymer composites: Manufacturing, properties, and applications. Polymers 2019;11(10). http://dx.doi.org/10.3390/polym11101667.

[5] Chawla KK. Composite materials. Cham: Springer International Publishing; 2019, http://dx.doi.org/10.1007/978-3-030-28983-6.

[6] Shao-Yun, Lauke B. Hybrid effects on tensile properties of hybrid short-glass-fiber-and short-carbon-fiber-reinforced polypropylene composites. J Mater Sci 36 2001.

[7] Ishikawa T, Amaoka K, Masubuchi Y, Yamamoto T, Yamanaka A, Arai M, et al. Overview of automotive structural composites technology developments in Japan. Compos Sci Technol 2018;155:221–46. http://dx.doi.org/10.1016/j.compscitech.2017.09.015.

[8] Feraboli P, Peitso E, Deleo F, Cleveland T, Stickler PB. Characterization of prepreg-based discontinuous carbon fiber/epoxy systems. J Reinf Plast Compos 2009;28(10):1191–214. http://dx.doi.org/10.1177/0731684408088883.

[9] Selezneva M, Lessard L. Characterization of mechanical properties of randomly oriented strand thermoplastic composites. J Compos Mater 2016;50(20):2833–51. http://dx.doi.org/10.1177/0021998315613129.

[10] Wei H, Nagatsuka W, Lee H, Ohsawa I, Sumimoto K, Wan Y, et al. Mechanical properties of carbon fiber paper reinforced thermoplastics using mixed discontinuous recycled carbon fibers. Adv Compos Mater 2018;27(1):19–34. http://dx.doi.org/10.1080/09243046.2017.1334274.

[11] Krause W, Henning F, Tröster S, Geiger O, Eyerer P. LFT-D — A process technology for large scale production of fiber reinforced thermoplastic components. J Thermoplastic Compos Mater 2003;16(4):289–302. http://dx.doi.org/10.1177/0892705703016004001.

[12] Gandhi U, Osswald TA, Goris S, Song Y-Y. Discontinuous fiber-reinforced composites: Fundamentals and applications. first ed.. Cincinnati: Hanser Publications; 2020.

[13] Bondy M, Pinter P, Altenhof W. Experimental characterization and modelling of the elastic properties of direct compounded compression molded carbon fibre/polyamide 6 long fibre thermoplastic. Mater Des 2017;122:184–96. http://dx.doi.org/10.1016/j.matdes.2017.03.010.

[14] Swolfs Y, Gorbatikh L, Verpoest I. Fibre hybridisation in polymer composites: A review. Composites A 2014;67:181–200. http://dx.doi.org/10.1016/j.compositesa.2014.08.027.

[15] Manders P, Bader MG. The strength of hybrid glass/carbon fibre composites. J Mater Sci 1981;(16):2233–45.

[16] Kretsis G. A review of the tensile, compressive, flexural and shear properties of hybrid fibre-reinforced plastics. Composites 1987;18(1):13–23. http://dx.doi.org/10.1016/0010-4361(87)90003-6.

[17] Bunsell AR, Harris B. Hybrid carbon and glass fibre composites. Composites 1974;5(4):157–64. http://dx.doi.org/10.1016/0010-4361(74)90107-4.

[18] Summerscales J, Short D. Carbon fibre and glass fibre hybrid reinforced plastics. Composites 1978;9(3):157–66. http://dx.doi.org/10.1016/0010-4361(78)90341-5.

[19] Fu S-Y, Mai Y-W, Lauke B, Yue C-Y. Synergistic effect on the fracture toughness of hybrid short glass fiber and short carbon fiber reinforced polypropylene composites. Mater Sci Eng A 2002;323(1–2):326–35. http://dx.doi.org/10.1016/S0921-5093(01)01383-1.

[20] Fu S-Y, Lauke B, Mai YW. Science and engineering of short fibre-reinforced polymer composites. In: Woodhead publishing series in composites science and engineering. 2nd ed.. Duxford England and Cambridge MA: Woodhead Publishing; 2019.

[21] Li Y-Q, Du S-S, Liu L-Y, Li F, Liu D-B, Zhao Z-K, et al. Synergistic effects of short glass fiber/short carbon fiber hybrids on the mechanical properties of polyethersulfone composites. Polym Compos 2019;40(S2):E1725–31.

[22] Yan X, Yang Y, Hamada H. Tensile properties of glass fiber reinforced polypropylene composite and its carbon fiber hybrid composite fabricated by direct fiber feeding injection molding process. Polym Compos 2018;39(10):3564–74. http://dx.doi.org/10.1002/pc.24378.

[23] Kehrer L, Wood JT, Böhlke T. Mean-field homogenization of thermoelastic material properties of a long fiber-reinforced thermoset and experimental investigation. J Compos Mater 2020;54(25):3777–99. http://dx.doi.org/10.1177/0021998320920695.

[24] Brylka B. Charakterisierung und modellierung der steifigkeit von langfaserverstärktem polypropylen [Ph.D. thesis], Karlsruhe: Karlsruher Institut für Technologie (KIT) and Karlsruher Institut für Technologie, http://dx.doi.org/10.5445/KSP/1000070061, URL http://nbn-resolving.de/urn:nbn:de:0072-700611.

[25] Schelleis C, Scheuring BM, Liebig WV, Hrymak AN, Henning F. Approaching polycarbonate as an LFT-D material: Processing and mechanical properties. Polymers 2023;15(9). http://dx.doi.org/10.3390/polym15092041, URL https://www.mdpi.com/2073-4360/15/9/2041.

[26] Kelly A, Tyson aW. Tensile properties of fibre-reinforced metals: Copper/tungsten and copper/molybdenum. J Mech Phys Solids 1965;13(6):329–50.

[27] Kim S-E, Ahn J-G, Ahn S, Park D-H, Choi D-H, Lee J-C, et al. Development of PA6/GF long-fiber-reinforced thermoplastic composites using pultrusion and direct extrusion manufacturing processes. Appl Sci 2022;12(10):4838.

[28] Zhu Y, Ma Y, Yan C, Xu H, Liu D, Chen G, et al. Improved interfacial shear strength of CF/PA6 and CF/epoxy composites by grafting graphene oxide onto carbon fiber surface with hyperbranched polyglycerol. Surf Interface Anal 2021;53(10):831–43.

[29] Sharma BN, Naragani D, Nguyen BN, Tucker CL, Sangid MD. Uncertainty quantification of fiber orientation distribution measurements for long-fiber-reinforced thermoplastic composites. J Compos Mater 2018;52(13):1781–97. http://dx.doi.org/10.1177/0021998317733533.

[30] Blarr J, Sabiston T, Krauß C, Bauer J, Liebig W, Inal K, et al. Implementation and comparison of algebraic and machine learning based tensor interpolation methods applied to fiber orientation tensor fields obtained from CT images. Comput Mater Sci 2023;228:112286. http://dx.doi.org/10.1016/j.commatsci.2023.112286, URL https://www.sciencedirect.com/science/article/pii/S092702562300280X.

[31] Feldkamp LA, Davis LC, Kress JW. Practical cone-beam algorithm. J Opt Soc Amer A 1984;1(6):612–9.

[32] Advani SG, Tucker CL. The use of tensors to describe and predict fiber orientation in short fiber composites. J Rheol 1987;31(8):751–84. http://dx.doi.org/10.1122/1.549945.

[33] Pinter P, Dietrich S, Bertram B, Kehrer L, Elsner P, Weidenmann KA. Comparison and error estimation of 3D fibre orientation analysis of computed tomography image data for fibre reinforced composites. NDT E Int 2018;95:26–35. http://dx.doi.org/10.1016/j.ndteint.2018.01.001.

[34] McCormick M, Liu X, Ibanez L, Jomier J, Marion C. ITK: Enabling reproducible research and open science. Front Neuroinform 2014;8. http://dx.doi.org/10.3389/fninf.2014.00013, URL https://www.frontiersin.org/articles/10.3389/fninf.2014.00013.

[35] Yoo TS, Ackerman MJ, Lorensen WE, Schroeder W, Chalana V, Aylward S, et al. Engineering and algorithm design for an image processing api: A technical report on ITK–the insight toolkit. Stud Health Technol Inf 2002;85:586–92.

[36] Blarr J, Kresin N, Krauß C, Weidenmann KA, Liebig WV, Elsner P, editors. Application of a tensor interpolation method on the determination of fiber orientation tensors from computed tomography images. Composites Meet Sustainability - Proceedings of the 20th European Conference on Composite Materials: Anastasios, Vassilopoulos, EPFL; 2022, http://dx.doi.org/10.5445/IR/1000155486, URL https://publikationen.bibliothek.kit.edu/1000155486.

[37] Blarr J. Dataset: FOT interpolation code and scans: 3D μct images of specimens of carbon fiber reinforced polyamide 6 plaque, fiber orientation tensor data of these images, and three python code files for two different algebraic and one machine learning based tensor interpolation algorithms. 2022, http://dx.doi.org/10.5445/IR/1000153725.

[38] Jack DA, Smith DE. The effect of fibre orientation closure approximations on mechanical property predictions. Composites A 2007;38(3):975–82. http://dx.doi.org/10.1016/j.compositesa.2006.06.016.

[39] Dray D, Gilormini P, Regnier G. Comparison of several closure approximations for evaluating the thermoelastic properties of an injection molded short-fiber composite. Compos Sci Technol 2007;67(7–8):1601–10. http://dx.doi.org/10.1016/j.compscitech.2006.07.008.

[40] Harris CR, Millman KJ, van der Walt SJ, Gommers R, Virtanen P, Cournapeau D, et al. Array programming with NumPy. Nature 2020;585(7825):357–62. http://dx.doi.org/10.1038/s41586-020-2649-2.

[41] Shepard D, editor. A two-dimensional interpolation for irregularly-spaced data. In: Proceedings of the 1968 23rd ACM national conference, (no. 517–524). 1968, http://dx.doi.org/10.1145/800186.810616.

[42] Barral M, Chatzigeorgiou G, Meraghni F, Léon R. Homogenization using modified Mori-Tanaka and TFA framework for elastoplastic-viscoelastic-viscoplastic composites: Theory and numerical validation. Int J Plast 2020;127:102632. http://dx.doi.org/10.1016/j.ijplas.2019.11.011.

[43] Christensen RM. Mechanics of composite materials. In: Dover civil and mechanical engineering, New York: Dover Publications; 2012, URL https://ebookcentral.proquest.com/lib/kxp/detail.action?docID=1894621.

[44] Aboudi J, Arnold SM, Bednarcyk BA. Micromechanics of composite materials. Elsevier; 2013, http://dx.doi.org/10.1016/C2011-0-05224-9.

[45] Chawla KK. Composite materials. Cham: Springer International Publishing; 2019, http://dx.doi.org/10.1007/978-3-030-28983-6.

[46] Yu W. An introduction to micromechanics. Appl Mech Mater 2016;828:3–24. http://dx.doi.org/10.4028/www.scientific.net/AMM.828.3.

[47] Voigt W. Ueber die Beziehung zwischen den beiden Elastizitätsconstanten isotroper Körper. Ann Phys, Lpz 1889;274(12):573–87. http://dx.doi.org/10.1002/andp.18892741206.

[48] Reuss A. Berechnung der fließgrenze von mischkristallen auf grund der plastizitätsbedingung für einkristalle. ZAMM - Z Angew Math Mech 1929;9(1):49–58. http://dx.doi.org/10.1002/zamm.19290090104.

[49] Parnell WJ, Calvo-Jurado C. On the computation of the Hashin–Shtrikman bounds for transversely isotropic two-phase linear elastic fibre-reinforced composites. J Engrg Math 2015;95(1):295–323. http://dx.doi.org/10.1007/s10665-014-9777-3.

[50] Liu B, Feng X, Zhang S-M. The effective Young's modulus of composites beyond the voigt estimation due to the Poisson effect. Compos Sci Technol 2009;69(13):2198–204. http://dx.doi.org/10.1016/j.compscitech.2009.06.004.

[51] Eshelby JD. The determination of the elastic field of an ellipsoidal inclusion, and related problems. Proc R Soc Lond. Ser A. Math Phys Sci 1957;241(1226):376–96. http://dx.doi.org/10.1098/rspa.1957.0133.

[52] Hashin Z. Analysis of composite materials—A survey. J Appl Mech 1983;50(3):481–505. http://dx.doi.org/10.1115/1.3167081.

[53] Pierard O, Friebel C, Doghri I. Mean-field homogenization of multi-phase thermo-elastic composites: A general framework and its validation. Compos Sci Technol 2004;64(10–11):1587–603. http://dx.doi.org/10.1016/j.compscitech.2003.11.009.

[54] Fritsch A, Hellmich C, Young P. Micromechanics-derived scaling relations for poroelasticity and strength of brittle porous polycrystals. J Appl Mech 2013;80(2):020905.

[55] Morin C, Vass V, Hellmich C. Micromechanics of elastoplastic porous polycrystals: Theory, algorithm, and application to osteonal bone. Int J Plast 2017;91:238–67.

[56] Gross D, Seelig T. Bruchmechanik. Berlin, Heidelberg: Springer Berlin Heidelberg; 2016, http://dx.doi.org/10.1007/978-3-662-46737-4.

[57] Qiu YP, Weng GJ. On the application of Mori-Tanaka's theory involving transversely isotropic spheroidal inclusions. Internat J Engrg Sci 1990;28(11):1121–37. http://dx.doi.org/10.1016/0020-7225(90)90112-V.

[58] Weng GJ. The theoretical connection between Mori-Tanaka's theory and the Hashin-Shtrikman-Walpole bounds. Internat J Engrg Sci 1990;28(11):1111–20. http://dx.doi.org/10.1016/0020-7225(90)90111-U.

[59] Lee D. Local anisotropy analysis based on the Mori-Tanaka model for multiphase composites with fiber length and orientation distributions. Composites B 2018;148:227–34. http://dx.doi.org/10.1016/j.compositesb.2018.04.050.

[60] Brylka B. 2017. http://dx.doi.org/10.5445/KSP/1000070061.

[61] Bauer JK, Böhlke T. On the dependence of orientation averaging mean field homogenization on planar fourth-order fiber orientation tensors. Mech Mater 2022;170:104307. http://dx.doi.org/10.1016/j.mechmat.2022.104307, URL https://www.sciencedirect.com/science/article/pii/S0167663622000886.

[62] Jiménez Segura N, Pichler BL, Hellmich C. Concentration tensors preserving elastic symmetry of multiphase composites. Mech Mater 2023;178:104555. http://dx.doi.org/10.1016/j.mechmat.2023.104555, URL https://www.sciencedirect.com/science/article/pii/S0167663623000017.

[63] Halpin JC. Effects of environmental factors on composite materials. 1969.

[64] Fu S-Y, Xu G, Mai Y-W. On the elastic modulus of hybrid particle/short-fiber/polymer composites. Composites B 2002;33(4):291–9. http://dx.doi.org/10.1016/S1359-8368(02)00013-6.

[65] Daniel IM, Ishai O. Engineering mechanics of composite materials. 2nd ed.. New York, NY: Oxford Univ. Press; 2006, URL http://www.loc.gov/catdir/enhancements/fy0635/2004065462-d.html.

[66] Christ N, Scheuring BM, Montesano J, Hohe J. HomoPy: A Python package for homogenization procedures in fiber reinforced polymers. J Open Source Softw 2023;8(87):5295. http://dx.doi.org/10.21105/joss.05295.

[67] Cox HL. The elasticity and strength of paper and other fibrous materials. Br J Appl Phys 1952;3(3):72–9. http://dx.doi.org/10.1088/0508-3443/3/3/302.

[68] Böhlke T, Brüggemann C. Graphical representation of the generalized Hooke's law. Technische Mech 2001;21(2):145–58.

[69] Schreyer L, Blarr J, Höger K, Meyer N, Kärger L. Generation of initial fiber orientation states for long fiber reinforced thermoplastic compression molding simulation. In: Composites meet sustainability : proceedings of the 20th European conference on composite materials, ECCM20. 26-30 June, 2022, Lausanne, Switzerland. Bd.: 4. ed.: A. Vassilopoulos. École Polytechnique Fédérale de Lausanne (EPFL); 2022, p. 687–94. http://dx.doi.org/10.5445/IR/1000155599.

[70] Barmpoutis A, Vemuri BC, Shepherd TM, Forder JR. Tensor splines for interpolation and approximation of DT-MRI with applications to segmentation of isolated rat hippocampi. IEEE Trans Med Imaging 2007;26(11):1537–46. http://dx.doi.org/10.1109/TMI.2007.903195.

[71] Fliegener S. Micromechanical finite element modeling of long fiber reinforced thermoplastics [Ph.D. thesis], Karlsruhe, Karlsruher Institut für Technologie (KIT), Diss., 2015; 2015.

[72] Wollan E. Glass & carbon fiber reinforcement combine in hybrid long fiber thermoplastic composites to bridge price & performance gap. Reinforced Plastics 2017;61(1):55–7. http://dx.doi.org/10.1016/j.repl.2015.09.007.

[73] Sharma M, Bijwe J, Singh K. Studies for wear property correlation for carbon fabric-reinforced PES composites. Tribol Lett 2011;43:267–73.